Redox Biology 71 (2024) 103086

Contents lists available at ScienceDirect

Redox Biology

journal homepage: www.elsevier.com/locate/redox

Iron/ROS/Itga3 mediated accelerated depletion of hippocampal neural stem cell pool contributes to cognitive impairment after hemorrhagic stroke

Xuyang Zhang [a,1], Huanhuan Li [a,1], Haomiao Wang [a,1], Qian Zhang [b], Xueyun Deng [e,a], Shuixian Zhang [a], Long Wang [a], Chao Guo [a], Fengchun Zhao [a], Yi Yin [a], Tengyuan Zhou [a], Jun Zhong [a], Hui Feng [a], Wei Chen [d], Jun Zhang [c], Hua Feng [a], Rong Hu [a,*]

[a] Department of Neurosurgery and Key Laboratory of Neurotrauma, Southwest Hospital, Third Military Medical University (Army Medical University), 400038, Chongqing, China
[b] Clinical Medical Research Center, Southwest Hospital, Third Military Medical University (Army Medical University), Chongqing, 400038, China
[c] Department of Neurobiology, College of Basic Medical Sciences, Third Military Medical University (Army Medical University), Chongqing, 400038, China
[d] Department of Radiology, Southwest Hospital, Third Military Medical University (Army Medical University), Chongqing, 400038, China
[e] Department of Neurosurgery, The Affiliated Nanchong Central Hospital of North Sichuan Medical College, Nanchong, 637000, China

ARTICLE INFO

Keywords:
Hemorrhagic stroke
ROS
Neural stem cell pool
Neurogenesis
Cognitive impairment

ABSTRACT

Hemorrhagic stroke, specifically intracerebral hemorrhage (ICH), has been implicated in the development of persistent cognitive impairment, significantly compromising the quality of life for affected individuals. Nevertheless, the precise underlying mechanism remains elusive. Here, we report for the first time that the accumulation of iron within the hippocampus, distal to the site of ICH in the striatum, is causally linked to the observed cognitive impairment with both clinical patient data and animal model. Both susceptibility-weighted imaging (SWI) and quantitative susceptibility mapping (QSM) demonstrated significant iron accumulation in the hippocampus of ICH patients, which is far from the actual hematoma. Logistical regression analysis and multiple linear regression analysis identified iron level as an independent risk factor with a negative correlation with post-ICH cognitive impairment. Using a mouse model of ICH, we demonstrated that iron accumulation triggers an excessive activation of neural stem cells (NSCs). This overactivation subsequently leads to the depletion of the NSC pool, diminished neurogenesis, and the onset of progressive cognitive dysfunction. Mechanistically, iron accumulation elevated the levels of reactive oxygen species (ROS), which downregulated the expression of Itga3. Notably, pharmacological chelation of iron accumulation or scavenger of aberrant ROS levels, as well as conditionally overexpressed Itga3 in NSCs, remarkably attenuated the exhaustion of NSC pool, abnormal neurogenesis and cognitive decline in the mouse model of ICH. Together, these results provide molecular insights into ICH-induced cognitive impairment, shedding light on the value of maintaining NSC pool in preventing cognitive dysfunction in patients with hemorrhagic stroke or related conditions.

1. Introduction

Intracerebral hemorrhage (ICH), a lethal subtype of stroke, is widely recognized as a major contributor to global mortality and disability. The incidence of ICH varies between 10 and 20% in western countries, whereas it exhibits an even higher prevalence of 30–40% in Asia [1–3]. Among patients diagnosed with ICH, about 19%–63.3% of them experience cognitive impairment within four years following the onset of ICH [4–10]. The cognitive impairment is associated with shorter average lifespan and diminished quality of life for those affected. Despite the gravity of this situation, research efforts have predominantly focused on post-ICH motor recovery, with relatively less attention given to post-ICH cognitive recovery. Understanding the underlying mechanisms and exploring treatment strategies for post-ICH cognitive impairment are still in its early stage of investigation.

Adult neurogenesis primarily occurs in two regions: the subgranular zone (SGZ) of dentate gyrus (DG) in the hippocampus and the subventricular zone (SVZ) [11,12]. Neural stem cells (NSCs) have the ability

* Corresponding author.
E-mail address: huchrong@tmmu.edu.cn (R. Hu).
[1] These authors contributed equally to this work.

https://doi.org/10.1016/j.redox.2024.103086
Received 4 January 2024; Received in revised form 11 February 2024; Accepted 11 February 2024
Available online 13 February 2024

to undergo self-renewing or differentiate into intermediate progenitor cells (IPCs), which ultimately mature into neurons or glial cells [11,13]. This process is known as neurogenesis and contributes to learning and memory. Impaired hippocampal neurogenesis has been associated with cognitive impairment, dementia, depression, epilepsy, and schizophrenia [14–16]. Some studies have indicated that stroke affects adult neurogenesis in the SVZ or DG [17–19]. However, the specific temporal and spatial patterns of hippocampal neurogenesis following ICH, as well as its impact on the NSC pool and cognitive function, remain largely unknown.

Iron plays a pivotal role in multiple biological function of the brain [20,21], while dysregulation of iron balance could induce neurotoxicity through various mechanisms [22,23]. Our previous studies have demonstrated that iron accumulation after ICH contributes to secondary brain damage via inflammatory reactions, oxidative stress, etc [24–33]. Whether local iron accumulation could affect the hippocampus and subsequently adult hippocampal neurogenesis and cognition after ICH remain elusive. In this study, our aim was to investigate the impact of basal ganglion ICH on adult hippocampal neurogenesis and cognition, as well as to explore the possible mechanisms involved. Clinical data showed an association between the level of iron accumulation in the hippocampus and cognitive impairment in ICH patients. Iron accumulation causes excessive ROS production and overactivation of NSCs in the early stage, subsequently downregulating Itga3, which leads to the depletion of the NSC pool, impaired neurogenesis and cognition following ICH.

2. Materials and methods

2.1. Clinical samples

The clinical study was approved by the Ethics Committee of the First Affiliated Hospital of the Army Medical University, and all patients who participated in the study signed written informed consent. In our study, we collected MMSE and MOCA scores from patients diagnosed with basal ganglia ICH. Cognitive impairment was confirmed if the MMSE score was below 27 and the MOCA score was below 26 [34–36]. Susceptibility weighted imaging (SWI) was obtained from the phase map of the SWI sequence [37]. For each subject, the hippocampus was selected from anterior to posterior, and six layers were chosen as the region of interest. Then, quantitative susceptibility mapping (QSM) analysis was conducted to enhance visualization and quantify the extent of iron accumulation in the hippocampus [38]. Briefly, the QSM reconstruction was implemented using the STISuite4 software package. The phase unwrapping step employed the Laplacian method to resolve phase ambiguities in the images. Background field removal was performed using the Variable-Shaped Kernel for Complex Harmonic Artifact Reduction and Phase Preserve (VSHARP) algorithm, which effectively eliminates background field distortions. Finally, the tissue susceptibility distribution was inverted using the STAR-QSM method, which incorporates a stripe artifact reduction technique, to obtain the final quantitative magnetic susceptibility map.

2.2. Mouse strains

The mouse strains used in our experiment included as following: C57BL/6J, Nestin-GFP, Nestin-CreER^{T2}, Rosa26R-CAG:tdTomato, Rosa26 Loci-CAG:floxed-STOP-Itga3CDS:EGFP. To label endogenous NSCs, we crossed Nestin-CreER^{T2} with Rosa26R-CAG:tdTomato. To conditionally overexpress Itga3 on NSCs, we crossed Nestin-CreER^{T2} with Rosa26 Loci-CAG:floxed-STOP-Itga3CDS:EGFP. All mice in this study were backcrossed to the C57BL/6J background for at least six generations. To induce recombination, adult mice (6–8 weeks) were intraperitoneally injected with tamoxifen (150 mg/kg for 5 days). Mice were housed in a relatively sterile environment with a 12-h light cycle at room temperature and controlled relative humidity. All animal experiments were conducted in compliance with China's animal welfare law for the protection of scientific research animals and were approved by the Army Medical University for the use of laboratory animals.

2.3. Animal models

The ICH model was referred to our previous study [29]. Briefly, mice were secured on the stereotaxic apparatus and anesthetized using isoflurane. The entire process consists of skin preparation, disinfection, cranium exposure and injection under strictly sterile conditions. After carefully drilling a burr hole, insertion of a needle was inserted on the right side of the skull without penetrating the meninges. The bregma served as a reference point, with coordinates of 2.0 mm to the right and 0.6 mm forward. A microinjection syringe was then inserted into the basal ganglia to a depth of 3.0 mm and 20 μL of nonheparinized autologous blood was injected at a velocity of 2 μL/min. Then, the needle was kept in place for 10 min before being slowly withdrawn. In Sham mice, the needle was inserted into the brain without injection. Following the injection, the incision was disinfected and sutured using silk sutures.

2.4. Isolation and culture of hippocampal neural stem cells

Improving upon previous methods [26,39], we breed mice in-house by housing males and females together. Fifteen days after birth, P15 mice were euthanized by cervical dislocation, and the whole brain tissue was placed in ice-cold Hank's balanced salt solution (HBSS). The hippocampus was dissected under a microscope, and the tissue was washed with pre-chilled PBS buffer. Papain enzyme was used to digest the tissue blocks, followed by termination of digestion with 10% FBS (Gibco, 10099141C). The tissue was gently triturated in DMEM/F12 (Gibco, C11330500 b t) medium, and the resulting cell suspension was cultured in neural stem cells (NSCs) culture medium, which consisted of DMEM/F12, 2% B27 (Gibco, Grand Island, NY), 20 ng/mL EGF (Peprotech, Rocky Hill, NJ), and 20 ng/mL FGF-2 (Peprotech, Rocky Hill, NJ). The cell suspension was passed through a 70 μm cell strainer, and NSCs culture medium was added. Subsequently, the cells were incubated in a dedicated cell culture incubator (37 °C, 5% CO_2). Upon the formation of suspended neurospheres, the cells were subjected to passaging. For the passaging procedure, the neurospheres were initially centrifuged to consolidate the cells, and subsequently, the supernatant was carefully discarded. Accutase® was utilized to dissociate the cells for 12 min in order to obtain single cells, with gentle agitation of the centrifuge tube during digestion to ensure thorough dissociation. The digestion was terminated by adding 2–3 mL of NSCs culture medium to prevent over-digestion and cell damage. The cells were then centrifuged at 300G, and the supernatant was discarded. The single cells were resuspended in fresh culture medium, and poly-L-ornithine (10 μg/mL) was used for pre-coating the culture surface for subsequent cell adhesion experiments.

2.5. EdU administration

For in vivo labeling of cell proliferation, EdU (Beyotime, ST067) was dissolved in PBS and intraperitoneally injected at a dose of 50 mg/kg 24 h prior to the experimental analysis. For in vivo cell differentiation labeling, EdU was injected at a dose of 200 mg/kg for 3 days and analyzed 30 days later. For in vitro cell proliferation labeling, EdU was added to the NSCs suspension at a final concentration of 10 μM and incubated for 4 h before analysis. To monitor the penetration of EdU, brain frozen slices or cell staining were performed according to the manufacturer's instructions (Beyotime, C0075S). Briefly, the corresponding working solution was prepared and incubated at 37 °C for 40 min, followed by immunostaining analysis.

2.6. Tamoxifen administration

To induce recombination, mice received tamoxifen (Sigma-Aldrich, T5648) daily for 5 days (180 mg/kg intraperitoneal injection, 30 mg/mL in 10% sunflower oil, Sigma-Aldrich).

2.7. Iron content assay

Tissue iron content in the hippocampus was determined using an enzyme-linked immunosorbent assay (ELISA) kit (BioAssay Systems). The procedure was performed according to the manufacturer's instructions. Briefly, mouse hippocampus was dissected and homogenized in 200 μL of tissue lysis buffer at 4 °C for 2 h, followed by centrifugation at 12,000 rpm for 10 min at room temperature. The supernatant was collected for measurement. Standard curve with different concentrations of iron was prepared according to the kit instructions. The diluted test samples were mixed with the working solution, incubated at 60 °C for 1 h, and then centrifuged at 12,000 rpm for 5 min. The supernatant was collected and mixed with 30 μL of iron ion detection reagent. It was then incubated at room temperature for 30 min and subsequently centrifuged at 12,000 rpm for 5 min. The absorbance at 550 nm was measured to determine the iron ion concentration in the tissue. The measurement of iron in CSF was performed as described in our previous study [40].

The iron level in CSF was measured using the Liquid Sample Total Iron Content Colorimetric Assay Kit (APPLYGEN). The main principle of this assay kit is based on the efficient conversion of iron into its ferrous form by a reducing agent. Subsequently, the ferrous iron reacts with ferricyanide to form a distinct purple-red colored compound. The concentration of this compound can be accurately determined using colorimetric analysis within the wavelength range of 540–580 nm.

2.8. Deferoxamine (DFO) and N-acetylcysteine (NAC) administration

In vivo, DFO (100 mg/kg, dissolved in saline, Sigma-Aldrich) and NAC (1 mg/kg, dissolved in saline, Sigma-Aldrich) were administered by intraperitoneal injection every 12 h for a total of 7 consecutive days. In vitro, NSCs was pretreated with DFO (5 μM) or NAC (1 μM) once.

2.9. Dihydroethidium (het) administration

The ROS-sensitive dye dihydroethidium (Het, 25 mg/kg, Sigma-Aldrich) was injected 4 h before analysis. Fluorescence intensity of brain sections was analyzed using Zen (Carl Zeiss, Weimar, Germany).

2.10. Immunohistochemistry

Saline was used for perfusion followed by 4% paraformaldehyde (PFA) for tissue fixation. The brain was dissected and immersed in 4% PFA overnight, and then equilibrated in 30% sucrose mixed to PBS buffer. Brain tissue was sectioned on the coronal plane at a thickness of 30 μm on frozen section machine. Serial sections of hippocampal dentate gyrus were found in 6-well plates filled with antifreeze.

Brain sections were incubated with 0.5% TritonX-100 at room temperature for 1 h, followed by fetal bovine serum blocking for 2 h, stained with the primary antibodies over night at 4 °C. The corresponding secondary antibodies were incubated at room temperature for 2 h. Primary antibodies as following: GFP (1:1000, Aves labs), GFP (1:500,Invitrogen), RFP (1:1000,abcam), rabbit *anti*-Nestin (1:100,abcam), mouse *anti*-Nestin (1:400,abcam), rabbit anti-Sox2 (1:100,abcam), rabbit *anti*-GFAP (1:400,CST), rabbit *anti*-Ki67 (1:400,CST), mouse *anti*-GFAP (1:400,CST), rabbit *anti*-MCM2 (1:800,CST), rabbit *anti*-DCX (1:800, CST), rabbit *anti*-NeuN (1:500,CST), rabbit anti-Ferritin (1:200,abcam), rabbit *anti*-Itga3 (1:400,abcam). Secondary antibodies as following: goat anti-chicken Alexa Fluor 488 (1:500, abcam), goat anti-mouse Alexa Fluor 488 (1:500, abcam), goat anti-rabbit Alexa Fluor 555 (1:500, abcam), goat anti-mouse Alexa Fluor 555 (1:500, abcam), goat anti-rabbit Alexa Fluor 594 (1:500, abcam), goat anti-rabbit Alexa Fluor 647 (1:500, abcam). Images were acquired on confocal system (LSM 880).

2.11. Fe^{2+} injections

In vivo, $FeCL_2$ was dissolved in saline at a concentration of 2 mM. Stereotaxic injection point in DG of hippocampus using the following coordinates relative to bregma: lateral, ± 1.7 mm; anteroposterior, −2.0 mm; ventral, −2.0 mm. To observe the effect of iron on stem cells pool and neurogenesis, we injected 1 μL of $FeCL_2$ solution into the DG or control injection of the same volume of saline. In vitro, NSCs were stimulated with 25 μM Fe^{2+} after 24 h of cellular resuscitation.

2.12. Lentiviral transfection

The procedures for Itga3 overexpress were performed according to the manufacturer's instruction. NSCs were infected with Itga3 sgRNA lentivirus at 20 MOI. The medium containing 3 μg/mL puromycin was replaced every 24 h. At the scheduled time point, the cells were harvested for further assays. The following target sequences were used in the present experiments:

Itga3 sgRNA: TTCTCCGAACGTGTCACGT.

2.13. RNA-seq and data analysis

We used 8-week-old Nestin-GFP mice as models (ICH group) and sham-operated mice (sham group) as controls. At 7 days after ICH, we harvested hippocampal stem cells from two groups of mice. Briefly, Nestin-GFP mice were killed by necking, and the hippocampal tissue was microscopically separated by an auxiliary microscope instrument and placed in cold HBSS buffer. The tissue was digested by papain and passed through a 70 μm filter. The cell suspensions were subsequently sorted at 20 psi with an 80 μm filter on a FACS Aria ll. GFP^+ cells were sorted directly into cryogenic cell lysates and stored in a −80 °C for sequencing use. The experiment was repeated 3 times with 6 mice in each group.

The RNA-seq library was constructed and sequenced using Smart-seq 2 technology. Briefly, lysed cells were thawed and placed in the SMART-Seq V 4 ultra Low Input RNA Kit to amplify RNA amplification. U The library was built using the Nextera XT toolkit. The RNA quantity and purity, as well as the percentage of sequencing reads mapped to the reference genome, were generally higher than 70% in this experiment.

FASTQC checks the quality of the raw reads and trims the reads using BTRIM64. The trimmed reads were mapped to the mouse genome using Tophat 2 and to mouse genes using RSEM. Expression levels for each gene were quantified in units per million transcripts (TPM) and the number of fragments per million fragments (FPKM) was plotted using RSEM (V1.2.15) with default parameters. Differential expression were identified when its log fold change>1.5 and $p < 0.05$, performed with DESeq2. The Gene Ontology database was used to explore the differential genes and the possible mechanisms of their biological processes.

2.14. RT-qPCR

Total RNA isolation from the animal tissues and cells were performed using Trizol® (Invitrogen) according to the manufacturer's instructions. The cDNA was reverse transcribed by ezDNase enzyme kit (Promega). RT-qPCR was performed with the QuantStudio Real-Time PCR system (Applied Biosystems). The primers used for qPCR are as follows:

Itga3:

Forward: 5′-ACCTTTACCCAGACCTGCTAGTA-3′

Reverse: 5′-GAACACAGGAGGTAGCTGTACAA-3′

Itgb3:

Forward: 5′-TGTCGTCAGCCTTTACCAGAATT-3′

Reverse: 5′-ACGTACTTCCAGCTCCACTTTAG-3′
Ctsj:
Forward: 5′-GAGCCAAATTGCAGCAGTTACTT-3′
Reverse: 5′-TGTCTCCACCATGTCTTCCTTTG-3′
Cts3:
Forward: 5′-GCGGACACAGATTGCATGTAATT-3′
Reverse: 5′-CTTCCGTCAACACAGTCCACTAG-3′
Epha1:
Forward: 5′-GCCTTACGCCAACTACACATTTA-3′
Reverse: 5′-GTGCCATTCTTCGTCCTGATTCA-3′
4930486L24Rik:
Forward: 5′-GCTGGACTGCATGGGATCTAATG-3′
Reverse: 5′-TGCACTTTCTACCTGGTCCTATG-3′
GAPDH:
Forward: 5′-AACGGGAAGCCCATACC-3′
Reverse: 5′-CATACTCAGCACCGGCCTCA-3′

2.15. Western blot

Tissue was lysed using RIPA lysate containing Protease inhibitor and phosphatase inhibitors (Roche). Protein samples were separated by 10% or 15% SDS-PAGE and then transferred to polyvinylidene difluoride (PVDF) membranes (Millipore). Subsequently, 10% skim milk is sealed at room temperature for 2 h. Afterward, they were incubated with rabbit anti-Ferritin (1:1000, CST), rabbit anti-SOD1 (1:1000, CST), rabbit anti-SOD2 (1:1000, CST), rabbit *anti*-Itga3 (1:500, Boster), rabbit *anti*-Itgb1 (1:1000, CST), rabbit *anti*-Laminin (1:1000, CST), rabbit *anti*-E-cadherin (1:1000, CST), mouse *anti*-GAPDH (1:1000, Santa Cruz Biotechnology), mouse *anti*-Tublin (1:1000, Santa Cruz Biotechnology) antibodies overnight at 4 °C. Secondary anti-mouse and anti-rabbit horseradish peroxidase (HRP)-conjugated antibodies (1:10,000, Boster) were used to conjoin the primary antibodies at room temperature for 2 h. Finally, blots were visualized by electrochemiluminescence (ECL) substrate (ThermoFisher). Signals were detected by Image Lab™ software (Bio-Rad), and analyzed by Image Lab™ software (Bio-Rad).

2.16. Behavioral tests

We evaluated the cognitive function of mice by Morris water maze (MWM), New Object Location (NOL) and New Object Recognition (NOR).

The MWM was divided into two stages: training and testing. For training stage, an invisible escape platform was located in the same spatial location 1 cm below the water surface independent of a subject's start position on a particular trial. Mice were placed in the water maze from 4 different starting positions. In this way, each animal would be able to determine the platform's location, and each animal was given 4 trials/day for consecutive 4 days. Twenty-four hours after the final training trial, a probe trial was performed, but the platform was removed.

NOL and NOR: Briefly, mice adapted to the environment alone for 10 min without objects. After 24 h, two identical same objects were placed on the side of the empty box and the mice were allowed to explore freely for 30 s. After 24 h, object recognition was tested by replacing a new object or location; the exploratory behavior of the mice was recorded with a VCR recorder for 10 min. New object or location preference expressed as the percentage of time spent exploring a new object or location versus the cumulative time spent exploring both objects.

2.17. Statistical analysis

All experimental data were analyzed using SPSS 23.0 and presented as mean ± SEM. Data were verified with the Shapiro-Wilk normality test. Independent-sample t-tests were used for numerical comparisons between the two groups, while one-way analysis of variance for comparisons between multiple groups, and tested with Tukey's post hoc test. $P < 0.05$ was considered statistically significant.

The influence of iron accumulation on cognitive impairment after ICH was analyzed using multivariate logistic regression. All variables with a significance level of less than 0.1 in the univariate analysis were included in the multivariate logistic regression analyses. Spearman correlation coefficient and linear regression analyses were adopted to investigate the associations between hippocampal iron level and post-ICH cognition.

3. Results

3.1. Cognitive impairment is associated with iron accumulation in the hippocampus following ICH

We initially conducted cognitive evaluation in patients with basal ganglion ICH using MMSE and MoCA tests, which are most common cognitive assessments [41–44]. Among 91 ICH patients enrolled, we identified 30 patients complicated with cognitive impairment based on both their MMSE (<27 points) and MoCA scores (<26 points). These cognitive assessments were obtained at a minimum of 6 months following the onset of ICH. We recruited 30 healthy participants matched with the ICH patients in age, sex, and education background (Table S1). Thus, MRI T1 (Fig. 1A) and SWI (Fig. 1B) data was obtained from 30 healthy individuals and 91 ICH patients. Upon analysis, we found that patients with ICH exhibited higher hippocampal phase shift values (denoting higher iron content) and lower MoCA and MMSE scores compared to the healthy control (Fig. 1B and C), suggesting that iron accumulation in hippocampus occurred after ICH and may contribute to cognitive impairment. By employing quantitative susceptibility mapping (QSM), a more precise method for assessing tissue iron levels, we found the significant iron accumulation in the hippocampus following ICH (Fig. 1D and E). Additionally, we detected the iron levels in the cerebrospinal fluid (CSF) of ICH patients over time (Fig. 1F). The findings showed that the increased iron level peaked at 7 days and continued at least 28 days after ICH.

To unravel the association between iron accumulation and cognitive impairment, we categorized the ICH patients into two groups based on the presence or absence of cognitive impairment (Table S2). Quantitative analysis showed a higher iron level in the patients with cognitive impairment than those without cognitive impairment (Fig. 1G and H). Moreover, both multivariate analysis (Table S3) and multiple linear regression analysis (Fig. 1I) revealed that elevated iron level is an independent risk factor for cognitive impairment after ICH with a negative correlation (Fig. 1G and H), suggesting that iron accumulation contributes to cognitive impairment after ICH.

To further dissect the link between iron accumulation in the hippocampus after ICH and cognitive impairment, we established striatum ICH model in mice, which mimics the most prevalent type of ICH (basal ganglion ICH) [1,2,45,46]. We evaluated the cognitive function in the chronic phase (at 90 days after ICH) using a water maze experiment. ICH mice showed decreased platform-crossing times compared with the Sham group. ICH mice also exhibited a significant delay in reaching the invisible platform and spent less time in the platform quadrant compared to the Sham mice (Figs. S1A and B). Similarly, novel object recognition (NOR) and novel object location (NOL) tests showed that the ICH group spent less time exploring new locations and objects, whereas the Sham group dedicated more time to these tasks (Figs. S1C and D). These results demonstrated that basal ganglion ICH leads to cognitive impairment, which is consistent with the findings in ICH patients.

In our previous studies, we revealed a significant accumulation of iron around hematomas following ICH [24,47]. However, whether iron accumulation occurs in distant areas such as hippocampus after striatum ICH remains unclear. To confirm the aforementioned data, we took advantage of western blotting to detect the expression of Ferritin in the hippocampus. The results showed that the expression of Ferritin in the hippocampus of ICH group was significantly elevated compared to the

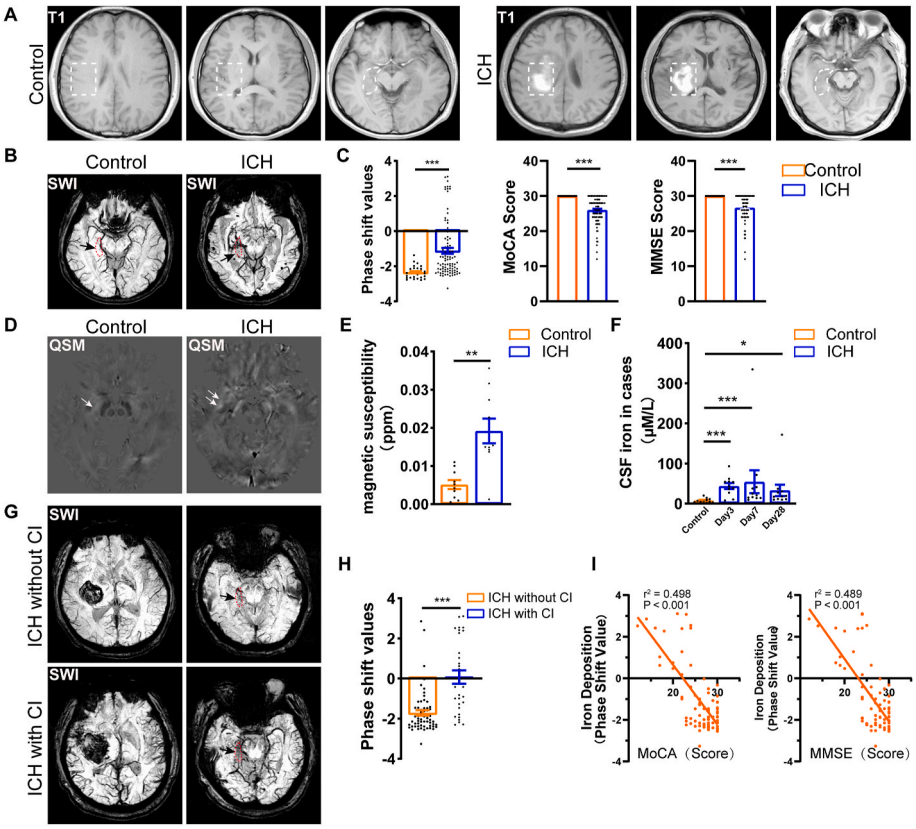

Fig. 1. Cognitive impairment is associated with iron accumulation in the hippocampus following ICH (A) Axial MRI images of basal ganglia (dashed rectangle) and hippocampus (dashed irregular) of healthy controls and ICH patients. (B–C) Axial SWI phase images showing the interesting region of healthy controls (n = 30) and ICH patients (n = 91). Black arrows indicate the regions of interest. Quantification and comparison of phase shift values used in quantitative analysis of iron content, MoCA score and MMSE score used to evaluated cognition of healthy controls and ICH patients. (D–E) Axial QSM reconstruction conducted from SWI phase of healthy controls (N = 10) and ICH patients (n = 10). White arrows indicate the regions of interest. Quantification and comparison of magnetic susceptibility of healthy controls and ICH patients. (F) Quantification and comparison of CSF iron level of healthy control (n = 11) and ICH patients (n = 11) at day 3, day 7 and day 28 after onset. (G–H) Axial SWI phase images showing hippocampal regions of interest in ICH with (n = 30) and without (n = 61) cognitive impairment (CI) for quantitative analysis of iron content. Black arrows indicate the regions of interest. Quantification and comparison of phase shift values used in quantitative analysis of iron content, MoCA score and MMSE score of ICH patients with or without cognitive impairments. (I) Spearman correlation coefficient and linear regression analyses were adopted to investigate the associations between Phase shift value and MoCA or MMSE score in ICH patients. (C, E, F) *P < 0.05; **P < 0.01; ***P < 0.001 vs corresponding Control. (H) ***P < 0.001 vs corresponding ICH without CI.

Sham group from day 3 to day 28, with the highest level observed on day 7 after ICH onset (Figs. S1E and F). Additionally, the quantification of total iron levels within the hippocampus using ELISA assay showed similar trend (Fig. S1G), providing direct evidence of iron accumulation in the hippocampus after ICH.

3.2. *Overactivation of hippocampal NSCs in the acute phase leads to NSC pool exhaustion and decreased neurogenesis after ICH*

Given the pivotal role of neurogenesis in the preservation of cognition, our study delved into the activation of NSCs and the consequential changes in neurogenesis subsequent to ICH. To assess NSCs activation, we administered intraperitoneal injections of EdU (50 mg/kg) 24 h before proliferation analysis using Nestin-GFP mice. Interestingly, the total number of rNSCs ($GFAP^+GFP^+$, referred to as radial NSCs) did not differ between the ICH and Sham group, while the number of proliferating rNSCs ($EdU^+GFAP^+GFP^+$) and proliferating GFP^+ cells (EdU^+GFP^+) were significantly increased at 3 and 7 days after surgical manipulation in the ICH group compared to the Sham group (Fig. 2B and C), indicating the increased activation and proliferation of hippocampal NSCs in the early acute phase of ICH. However, at 28 days and 90 days after ICH, the number of rNSCs ($GFAP^+GFP^+$), proliferating rNSCs ($EdU^+GFAP^+GFP^+$), and proliferating GFP^+ cells (EdU^+GFP^+) were found to be sharply decreased (Fig. 2B and C). Furthermore, we used MCM2, a marker of proliferating cells, to validate the activation and proliferation pattern of hippocampal NSCs. Similarly, we found $MCM2^+$ rNSCs increased at 3- and 7-days post-ICH, followed by a decrease at 28 days and 90 days post-ICH compared to the Sham control (Fig. 2D and E). These data suggest that ICH may induce excessive proliferation of rNSCs during the acute phase, which later leads to the reduction of total number of rNSCs. In addition, the ratio of $EdU^+Ki67^+GFP^+$ cells, representing cells that entered cell cycle, increased in the ICH group at 7 days compared to the Sham group (Fig. 2F–H), indicating that more NSCs entering cell cycle during the acute phase of ICH.

NSCs possess the ability of giving rise to neurons called neurogenesis [12,16,48,49]. In order to assess whether ICH-induced NSCs overactivation impacts neurogenesis over time, we administered EdU to track the proliferating cells at 60 days after ICH, followed by double immunostaining with NeuN and EdU. The data showed that profound diminished neurogenesis was observed (Fig. 2I and J). This finding suggest that ICH causes reduced hippocampal neurogenesis in the chronic phase.

Taken together, these results suggest that during the early stage, ICH may induce overactivation and proliferation of hippocampal NSCs, leading to a putative premature exhaustion of the NSC pool and a subsequent decreased neurogenesis over time.

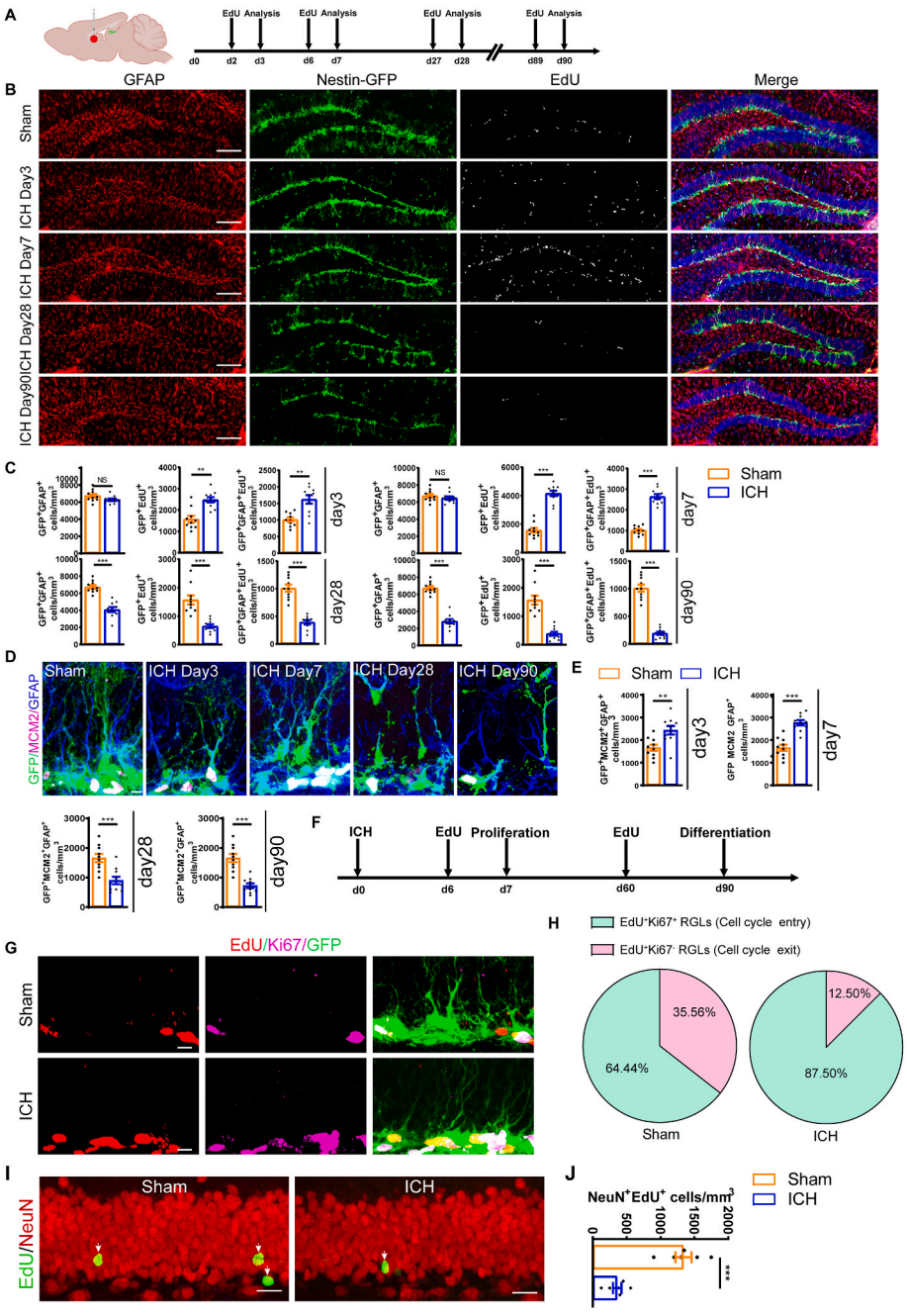

Fig. 2. Overactivation of hippocampal NSCs in the acute phase of ICH leads to NSC pool exhaustion and decreased neurogenesis after ICH (A) Schematic diagram of the ICH model, as well as experimental timeline for EdU administration and cell proliferation analysis. (B) Representative images of brain section stained with EdU, GFAP, and genetically labeled GFP in the DG of ICH mice at 3, 7, 28 and 90 days after ICH. Scale bar = 100 μm. (C) Quantification of numbers of rNSCs (GFP^+GFAP^+), proliferating GFP^+ (GFP^+EdU^+) and proliferating rNSCs ($GFP^+GFAP^+EdU^+$) cells from B. (n = 10 for each group). (D) Representative images of brain section stained with MCM2, GFAP, and genetically labeled GFP in the DG of ICH mice at 3, 7, 28 and 90 days after ICH. Scale bar = 5 μm. (E) Quantification of numbers of proliferating rNSCs ($GFP^+GFAP^+MCM2^+$) cells from D. (n = 10 for each group). (F) Experiments timeline for cell proliferation and differentiation analysis of ICH group. (G) Representative images of brain section stained with EdU, Ki67, and genetically labeled GFP in the DG of ICH mice at 7 days after ICH. Scale bar = 10 μm. (H) Quantified percentage of $GFP^+EdU^+Ki67^+$ (representing cells that entered cell cycle) and $GFP^+EdU^+Ki67^-$ (representing cells that exited cell cycle) cells from G. (n = 4 per group). (I) Representative images of brain section stained with EdU and NeuN in the DG of ICH mice at 90 days after ICH. White arrows indicate $NeuN^+EdU^+$ (adult-born neurons) cells. Scale bar = 20 μm. (J) Quantification of numbers of $NeuN^+EdU^+$ cells from J. (n = 6 for each group). (C, E, H, G) *P < 0.05; **P < 0.01; ***P < 0.001 vs corresponding Sham. Each experiment was repeated at least 3 times independently.

3.3. Iron accumulation is involved in ICH-induced overactivation and exhaustion of the NSC pool

Having established the occurrence of iron deposition in the hippocampus following ICH, our inquiry turned towards investigating whether such deposition is similarly augmented on NSCs within the hippocampus. To detect whether iron deposits in hippocampal NSCs, we measured the iron level in the NSCs of the hippocampus isolated from Nestin-GFP mice using FACS. The data showed that the intracellular iron level in the hippocampal NSCs was obviously increased following ICH compared to the Sham group (Fig. S1H), suggesting a remarkable iron accumulation in the NSCs of hippocampus after ICH.

Then, we asked whether iron accumulation in NSCs affects their activation and subsequent neurogenesis in adult hippocampus. To probe into the causal relationship between iron accumulation and ICH-induced overactivation and exhaustion of the NSC pool, deferoxamine (DFO), an iron chelator, was used to treat ICH mice via continuous intraperitoneal injection for 7 days (100 mg/kg). We investigated the alteration of the NSC pool in the hippocampus (Fig. 3A). The data showed that the administration of DFO significantly reduced the number of proliferating rNSCs ($EdU^+GFAP^+GFP^+$) compared to ICH at 3 and 7 days (Fig. 3B and C). As a result, the total number of rNSCs ($GFAP^+GFP^+$), proliferating rNSCs ($EdU^+GFAP^+GFP^+$) were significantly restored at 28 days and 90 days post-ICH in the DFO-treated group compared to the vehicle-treated group (Fig. 3B and C). Similarly, the number of $MCM2^+$ rNSCs proliferating progenitors were found to be decreased at 3 and 7 days in the

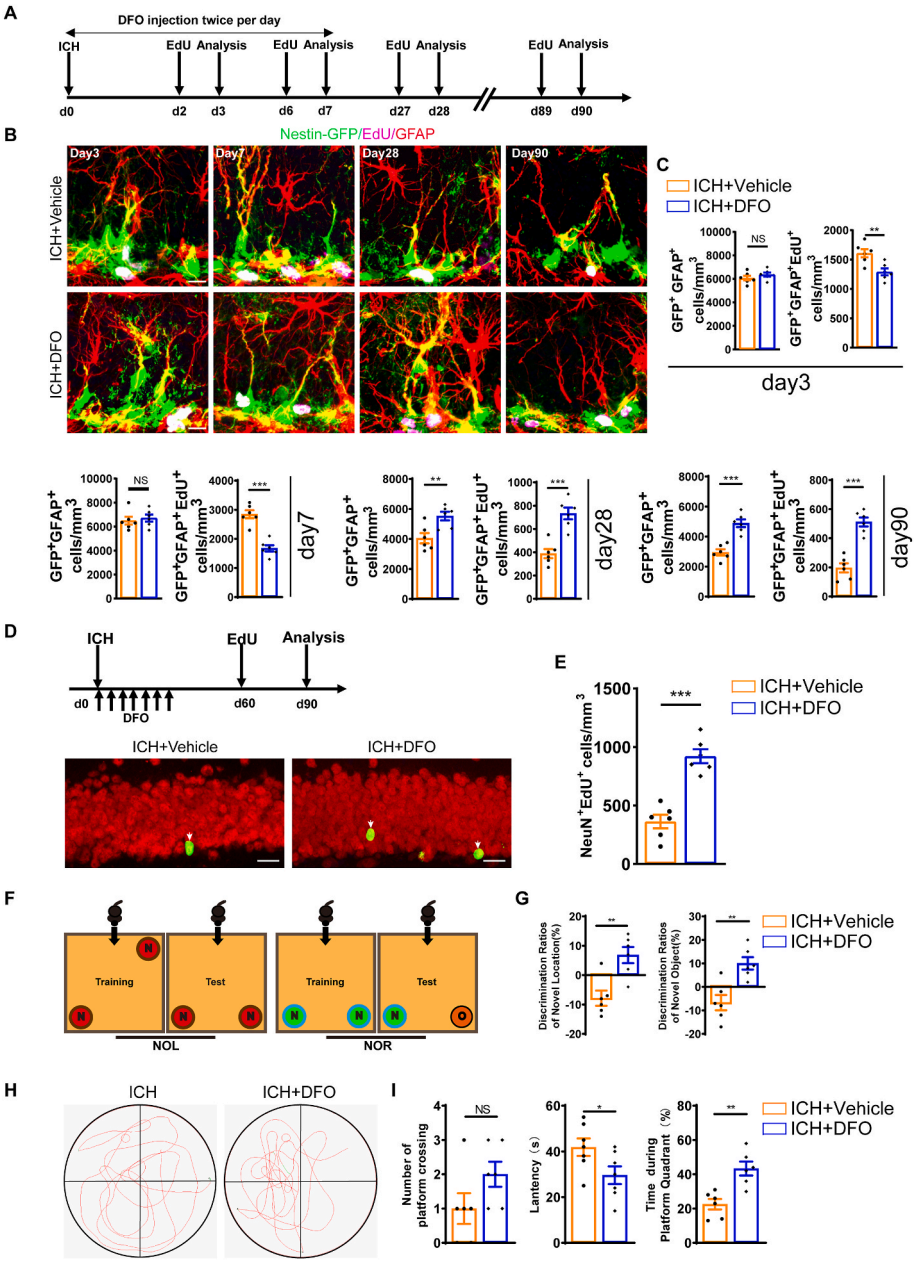

Fig. 3. Iron accumulation is involved in ICH-induced overactivation and exhaustion of the NSC pool (A) Schematic diagram of the ICH model, as well as experimental timeline for cell proliferation analysis of ICH group with or without DFO treatment. (B) Representative images of brain section stained with EdU, GFAP, and genetically labeled GFP in the DG at 3, 7, 28 and 90 days in ICH mice with or without DFO treatment. Scale bar = 10 μm. (C) Quantification of numbers of rNSCs (GFP^+GFAP^+) and proliferating rNSCs ($GFP^+GFAP^+EdU^+$) cells from B. (n = 6 for each group). (D) Experiments timeline for cell differentiation analysis of ICH + Vehicle and ICH+DFO group. Representative images of brain section stained with EdU and NeuN in the DG of ICH mice with or without DFO treatment at 90 days after ICH. White arrows indicate $NeuN^+EdU^+$ (adult-born neurons) cells. Scale bar = 20 μm. (E) Quantification of numbers of $NeuN^+EdU^+$ cells from F. (n = 6 for each group). (F) Schematic diagram of novel object location and novel object recognition test. (G) Quantification of the ratio of exploration time on novel objective location and novel object recognition in ICH mice with or without DFO treatment at 90 days after ICH. (n = 6 for each group). (H) Representative images of the swimming path of ICH + Vehicle and ICH + DFO during the probe trial test in Morris water maze test at 90 days after ICH. (I) Platform-crossing times of ICH + Vehicle and ICH + DFO mice during probe trial test. Escape latency of probe trial test of ICH + Vehicle and ICH + DFO mice. Duration of stay in the platform quadrant. (n = 6 for each group). (C, E, J, I) *P < 0.05; **P < 0.01; ***P < 0.001 vs corresponding ICH + Vehicle. NS = no significance. Each experiment was repeated at least 3 times independently.

DFO group compared to the vehicle group, but it was restored at 28 days and 90 days (Figs. S2B and C). These findings indicate that chelation of excessive hippocampal iron following ICH ameliorates the overactivation of NSCs, thereby preserving a stable NSC pool.

Next, we utilized double staining of EdU and NeuN to examine whether DFO treatment alleviates the decreased neurogenesis caused by ICH. The data showed that DFO treatment boosted more adult-born neurons than vehicle treatment over time (Fig. 3D and E). These findings indicate that impaired neurogenesis following ICH is mediated by iron accumulation. Finally, to further elucidate whether the effect of DFO on NSC pool and neurogenesis could account for the improvement in cognition, we evaluated the cognitive function of ICH mice using NOR/NOL and water maze tests. The results demonstrated that treatment with DFO was able to improve the cognitive impairment induced by ICH (Fig. 3F–I). Thus, these data suggest that iron accumulation is required for ICH-induced overactivation and exhaustion of the NSC pool, thereafter impaired neurogenesis and cognition.

3.4. Iron injection into hippocampus leads to overactivation and exhaustion of the NSC pool

To examine whether iron accumulation is sufficient to elicit early overactivation followed by exhaustion of NSCs, we injected iron into the hippocampus of normal mice. 1 μL of saline was delivered into the hippocampus as the Sham group, and 1 μL of $FeCl_2$ (2 mM) with or without the administration of DFO as the experimental group, respectively (Fig. S3A). First, we counted the number of EdU^+ cells in the SGZ of the DG, and found an increased number of proliferating cells (EdU^+) at 7 days after $FeCl_2$ injection (Figs. S3B and C). However, the number of proliferating cells (EdU^+) obviously decreased at 90 days (Figs. S3B and D). Notably, chelating iron alleviated proliferation at 7 days and restored the number of proliferating cells (EdU^+) in the SGZ of DG at 90 days (Figs. S3B–D). Furthermore, we observed the activation of NSCs and its dynamic changes in their pool after $FeCl_2$ injection. At 7 days after injection, the $FeCl_2$ group showed a significant increase in the

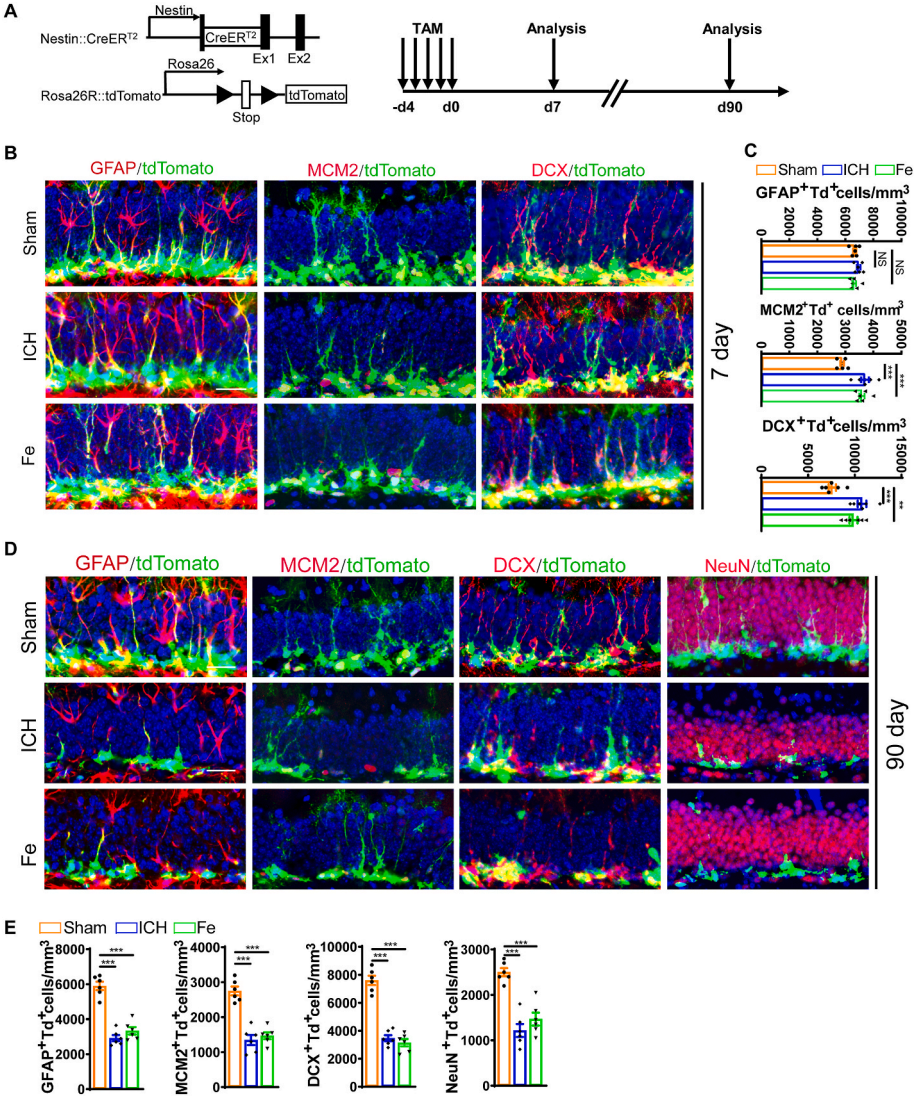

Fig. 4. Lineage tracing confirms the overactivation and subsequent exhaustion of NSC pool with impaired neurogenesis after ICH or iron injection (A) Schematic diagram and experimental timeline for the tamoxifen-induced Nestin:CreER^{T2}-mediated lineage tracing in mice. (B) Representative images of brain section stained with GFAP, MCM2, DCX and genetically labeled tdTomato in the DG of ICH group and $FeCl_2$ injected group at 7 days after ICH or $FeCl_2$ injection. Scale bar = 20 μm. (C) Quantification of numbers of rNSCs ($GFAP^+Td^+$), proliferating rNSCs ($MCM2^+Td^+$) and newborn neurons (DCX^+Td^+) from B. (n = 6 for each group). (D) Representative images of brain section stained with GFAP, MCM2, DCX, NeuN and genetically labeled tdTomato in the DG of ICH group and $FeCl_2$ injected group at 90 days after ICH or $FeCl_2$ injection. Scale bar = 20 μm. (E) Quantification of numbers of rNSCs ($GFAP^+Td^+$), proliferating rNSCs ($MCM2^+Td^+$), newborn neurons (DCX^+Td^+) and adult-born neurons ($NeuN^+Td^+$) from D. (n = 6 for each group). (C, E) **P < 0.01; ***P < 0.001 vs corresponding Sham. NS = no significance. Each experiment was repeated at least 3 times independently.

number of proliferating rNSCs ($EdU^+GFAP^+GFP^+$) and proliferating progenitors ($GFAP^+GFP^+MCM2^+$), compared to the Saline group (Figs. S3E–H). After 90 days, the $FeCl_2$ group exhibited a sharp decrease in the number of rNSCs ($GFAP^+GFP^+$), proliferating rNSCs ($EdU^+GFAP^+GFP^+$ and $GFAP^+GFP^+MCM2^+$), compared to the Sham group (Figs. S3E–H). However, using DFO to chelate iron markedly reversed the overactivation of NSCs in the acute phase, followed by the depletion of the NSC pool in the chronic phase (Figs. S3E–H). Additionally, the ratio of EdU + $Ki67^+GFP^+$ cells increased in $FeCl_2$ group, which was reversed by DFO treatment (Figs. S3I–J). Finally, we observed neurogenesis in this context. As shown in Figs. S3L and S3M, $FeCl_2$ decreased the number of adult-born neurons, whereas DFO treatment palliated this effect. Altogether, these above data suggest that the iron accumulation after ICH plays a central role in the early overactivation of NSCs followed by exhaustion of NSC pool and abnormal neurogenesis, which could be markedly diminished by iron chelation.

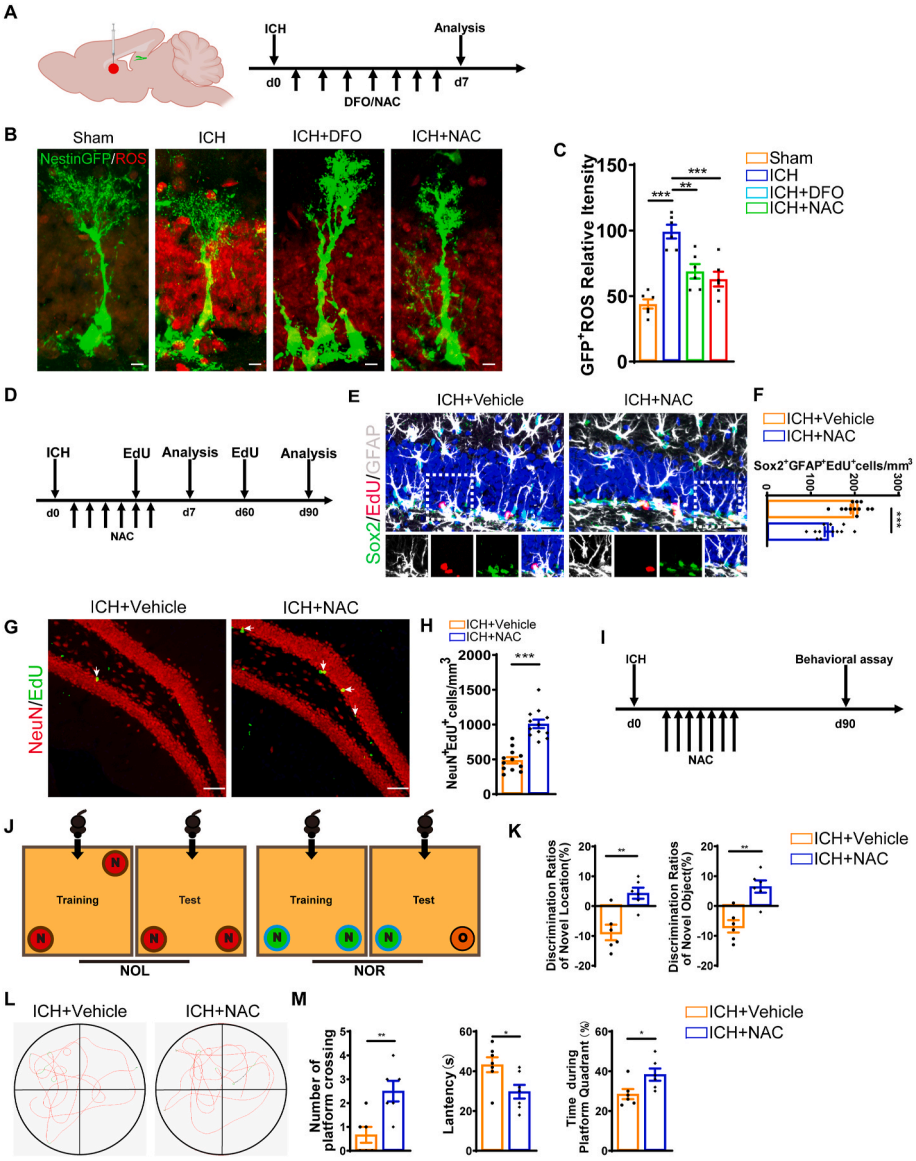

Fig. 5. Elevated ROS level mediated the effect of iron accumulation on NSC pool and neurogenesis after ICH (A) Schematic diagram of the ICH model and experimental timeline for ROS analysis of ICH mice. (B) Representative images of brain section stained with ROS and genetically labeled Nestin-GFP in DG of Sham, ICH, ICH + DFO and ICH + NAC group at 7 days after ICH. Scale bar: 5 μm. (C) Quantification of ROS fluorescence intensity from B. (n = 6 for each group). (D) Experiments timeline for cell proliferation analysis and neurogenesis trace by an EdU pulse chase in ICH mice with or without NAC treatment at 7 days after ICH. Scale bar = 20 μm. (E) Representative images of brain section stained with rNSCs (Sox2, EdU and GFAP) in the DG of ICH mice with or without NAC treatment at 7 days after ICH with or without NAC treatment. Scale bar = 20 μm. (F) Quantification of numbers of $Sox2^+GFAP^+EdU^+$ cells from E. (n = 12 for each group). (G) Representative images of brain section stained with NeuN, EdU and DAPI in the DG of ICH mice with or without NAC treatment at 90 days after ICH. Scale bar = 20 μm. (H) Quantification of numbers of $NeuN^+EdU^+$ (adult-born neurons) cells from G. (n = 12 for each group). (I) Experiments timeline for behavioral tests of ICH mice with or without NAC treatment. (J) Schematic diagram of novel object location and novel object recognition test. (K) Quantification of the ratio of exploration time on novel objective location and novel object recognition in ICH + Vehicle and ICH + NAC mice at 90 days after ICH. (n = 6 for each group). (L) Representative images of the swimming path of ICH + Vehicle and ICH + NAC mice during the probe trial test in Morris water maze test at 90 days after ICH. (M) Platform-crossing times of ICH + Vehicle and ICH + NAC during probe trial test. Escape latency of probe trial test of ICH + Vehicle and ICH + NAC mice. Duration of stay in the platform quadrant. N = 6 for each time point in each group. (C) **P < 0.01; ***P < 0.001 vs corresponding ICH. (F, H, K, M) *P < 0.05; **P < 0.01; ***P < 0.001 vs corresponding ICH + Vehicle. Each experiment was repeated at least 3 times independently.

3.5. Lineage tracing confirms the overactivation and subsequent exhaustion of NSC pool with impaired neurogenesis after ICH or iron injection

In order to dissect the activation and depletion of the hippocampal NSC pool and their lineage progression after ICH or $FeCl_2$ injection, we crossed Nestin:CreERT2 mice with Rosa26R-CAG:Tdtomato mice to label endogenous NSCs and perform lineage tracing (Fig. 4A). Tamoxifen (TAM) was administered intraperitoneally for a consecutive period of 5 days, and Tdtomato expression (Td^+) was observed in Nestin:CreERT2-derived endogenous NSCs in the DG. Three models were established, including Sham, ICH and $FeCl_2$ injection groups. Seven days after surgical operation, there was an obvious increase in proliferating progenitors (Td^+MCM2^+) and immature neurons (Td^+DCX^+) in the ICH and $FeCl_2$ groups, while the number of rNSCs (Td^+GFAP^+) remained unchanged (Fig. 4B and C). Thus, during the early stage of ICH, iron accumulation in the hippocampus promoted the transition of NSCs into mitotic progenitors and immature neurons without affecting the NSC pool. However, after 90 days, we found that the number of rNSCs (Td^+GFAP^+), proliferating progenitors (Td^+MCM2^+), immature neurons (Td^+DCX^+), mature neurons (Td^+NeuN^+) reduced obviously in both ICH and $FeCl_2$ group (Fig. 4D and E) compared with the Sham group. Therefore, these results further support our claim that ICH induces overactivation of NSCs in the early phase, resulting in the exhaustion of NSC pool and impairments in hippocampal neurogenesis.

3.6. Elevated ROS level mediated the effect of iron accumulation on NSC pool and neurogenesis after ICH

Previous studies have demonstrated the occurrence of sustained oxidative stress after ICH [50,51]. We hypothesized that iron accumulation in the hippocampus following ICH may also induce excessive ROS production as well, thereby leading to abnormal NSCs activation and consequential neurogenesis. To test this hypothesis, DFO and NAC (N-acetylcysteine, a ROS scavenger) were used to treat ICH mice twice per day via intraperitoneal injection (Fig. 5A). After 7 days, we found that the fluorescence intensity of ROS in the ICH groups was significantly higher compared to the Sham group. However, the ROS accumulation was alleviated by treatment with DFO or NAC (Fig. 5B and C). To provide further evidence, we took advantage of cultured hippocampal NSCs to quantitatively detect the level of ROS. We found that Fe^{2+} treatment significantly increased the production of ROS compared with the Control group. However, treatment with DFO or NAC reversed iron-induced excessive ROS production (Figs. S4B and C).

To explore whether iron-induced ROS production leads to the overactivation of NSCs and subsequently impaired neurogenesis, we examined the population of rNSCs ($Sox2^+GFAP^+$) and tracked their proliferation and differentiation after ROS scavenging (Fig. 5D). Compared to the vehicle group, the NAC-treated group showed attenuated excessive activation of rNSCs ($Sox2^+EdU^+GFAP^+$) (Fig. 5E and F) and increased the number of newly generated neurons ($NeuN^+EdU^+$) at 90 days post-ICH (Fig. 5G and H). In vitro study showed that both DFO and NAC also mitigated increased proliferation of NSCs (Figs. S4D and E), which mimics NSCs overactivation after ICH. Subsequently, to examine whether the clearance of ROS improves cognitive function in ICH mice, we administered NAC continuously for 7 days and subsequently conducted NOR/NOL and water maze test. NOR and NOL test showed that the NAC treated group required more time to explore new locations and objects, whereas the ICH group spent less time on these tasks (Fig. 5J and K). Additionally, in water maze test, ICH mice treated with NAC showed increased platform-crossing times, decreased latency reaching the invisible platform and spent more time in the platform quadrant compared to the ICH mice (Fig. 5L and M). These results indicate that scavenging ROS mitigates the effect of ICH on the exhaustion of NSC pool and abnormal neurogenesis, thereof reversing the cognitive impairment after ICH.

3.7. $Fe2^+$-ROS-Itga3 pathway is involved in the process of NSC pool exhaustion and abnormal neurogenesis

To further unravel the molecular mechanisms underlying the exhaustion of NSC pool caused by iron accumulation after ICH, we conducted RNA sequencing on Nestin-GFP^+ cells isolated from the hippocampus at 7 days after the ICH (Fig. 6A–D). A total of 30,871 genes were identified, among which 631 genes exhibited significant differential expression between the two groups. Out of these, 433 genes were upregulated, whereas 198 genes were downregulated (Fig. 6A). To identify the main changes of in vivo NSCs after ICH, we employed protein-protein interaction network analysis to elucidate the interaction among the differentially expressed genes (Fig. 6B). The results suggest that the inner biological process may be associated with oxidative stress and crosstalk between cell group and extracellular matrix. Additionally, GO enrichment analysis was performed to identify the most significant biological process, molecular function, and cellular component associated with the differentially expressed genes (Fig. 6C). Significantly, the biological process of "fibronectin binding" emerged as the most enriched term, while other terms from the molecular function and cellular component categories also lend support to the notion that this process may be linked to dynamic changes within the niche. Heat map was generated to visualize the differentially expressed genes involved in "fibronectin binding" (Fig. 6D) and found a set of genes Itga3, Epha1, Ctsj, Cts3, Itgb3, and 4930486L24RiK. Following this, we validated the set of candidate genes both in vivo and in vitro through RT-qPCR analysis (Fig. 6E and F). The data demonstrated that Itga3 was the most significantly differentially expressed gene. Collectively, these findings suggest that Itga3 might be involved in the process of ICH-induced exhaustion of NSC pool.

Itga3 is a member of integrin family [52]. We then determined whether other integrin member such as Itgb1 expression was influenced by ICH or Fe^{2+} treatment, we employed western blotting assay to detect the change of Itgb1 expression. The data showed no significant change of Itgb1 expression compared to the control group (Figs. S6A and B). In addition, we also detected the expression of other cell adhesion molecules such as Laminin and *E*-cadherin. The results showed that treatment with Fe^{2+} did not alter the expression of Laminin and *E*-cadherin in NSCs (Figs. S6A and B). These results imply that Itga3 is specifically involved in the process of iron-induced NSCs state changes.

Subsequently, we conducted in vitro experiments with cultured NSCs to explore the upstream or downstream regulatory relationships between Fe^{2+}, ROS, and Itga3. Upon exposure of NSCs to Fe^{2+}, the expression of SOD1, SOD2, and Itga3 was downregulated (Fig. 6G and H). However, DFO treatment reversed the expression levels of SOD1, SOD2, and Itga3 (Fig. 6G and H). Similarly, NAC treatment restored the expression of Itga3 which decreased after Fe^{2+} exposure (Fig. 6I and J). Finally, we constructed lentivirus to overexpress Itga3 in cultured NSCs. As shown in Fig. 6K and L, overexpression of Itga3, proved by RT-PCR assay (Figs. S6C and D), indeed rescued the decreased expression of Itga3 upon Fe^{2+} stimulation, but did not change the protein level of SOD1, SOD2, and Ferritin (Fig. 6K and L). Interestingly, overexpression of Itga3 has no effect on the proliferation of NSCs under normal condition (Figs. S6E and F). Together, these findings suggest that iron accumulation in the hippocampus after ICH leads to elevated production of ROS, thereafter decreases the expression of Itga3, resulting in exhaustion of NSC pool.

3.8. Conditional overexpression of Itga3 attenuates NSC pool exhaustion and cognitive impairment following ICH

To validate the role of Itga3 in the exhaustion of NSC pool and abnormal neurogenesis induced by ICH. We crossed Nestin:CreERT2 mice with Rosa26Loci-CAG:Itga3CDS$^{flox/flox}$:EGFP mice to generate conditionally overexpressed Itga3 mice (Fig. 7A). At 90 days after surgical manipulation, we examined hippocampal NSC pool and

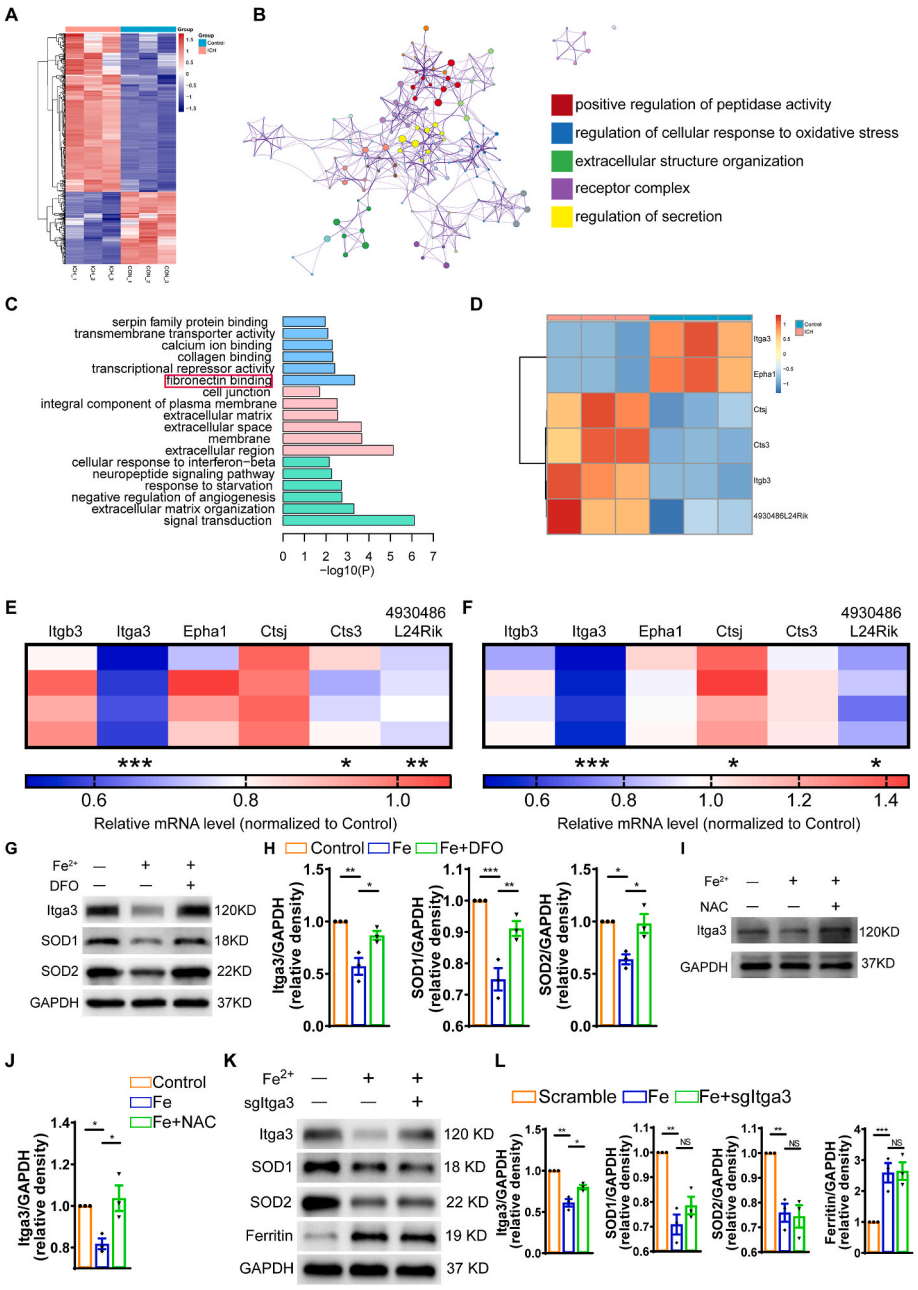

Fig. 6. Fe^{2+}-ROS-Itga3 pathway is involved in the process of NSC pool exhaustion and abnormal neurogenesis (A) Heatmap of total 631 differentially expressed genes between Control and ICH group at 7 days after ICH. (B) Protein-Protein interaction network of differentially expressed genes between Control and ICH group at 7 days after ICH. (C) Gene Ontology enrichment of differentially expressed genes between Control and ICH at 7 days after ICH. (D) Heatmap of PTM value of mRNA selected from differentially expressed genes included in fibronectin binding term. (E) Quantitative PCR validation of selected genes associated with fibronectin binding on independent samples of GFP^+ cells isolated from Control and ICH mice at 7 days after ICH. (n = 4 for each group). (F) Quantitative PCR validation of selected genes associated with fibronectin binding of cultured NSCs from Control and Fe^{2+} treated group. (n = 4 for each group). (G–H) Itga3, SOD1, SOD2 and GAPDH protein expression of cultured NSCs from Control and Fe^{2+}, Fe^{2+}+DFO group. Semi-quantitative analysis of WB results. GAPDH was served as the internal control. (n = 3 for each group). (I–J) Itga3 and GAPDH protein expression of cultured NSCs from Control and Fe^{2+}, Fe^{2+}+NAC group. Semi-quantitative analysis of WB results. GAPDH was served as the internal control. (n = 3 for each group). (K–L) Itga3, SOD1, SOD2, Ferritin and GAPDH protein expression of cultured NSCs from Control and Fe^{2+}, Fe^{2+}+sgItga3 group. Semi-quantitative analysis of WB results. GAPDH was served as the internal control. (n = 3 for each group). (E) *P < 0.05; **P < 0.01; ***P < 0.001 vs corresponding Sham. (F) *P < 0.05; **P < 0.01; ***P < 0.001 vs corresponding Control. (H, J, L) *P < 0.05; **P < 0.01; ***P < 0.001 vs corresponding Fe. NS = no significance. Each experiment was repeated at least 3 times independently.

neurogenesis. The data showed that the number of rNSCs (GFP^+GFAP^+), proliferating progenitor cells (GFP^+MCM2^+) and immature neurons (GFP^+DCX^+) obviously decreased after ICH (Fig. 7B and C). However, Itga3 overexpression in the NSCs ameliorated the decline in the number of rNSCs (GFP^+GFAP^+), proliferating progenitor cells (GFP^+MCM2^+), and immature neurons (GFP^+DCX^+) induced by ICH (Fig. 7B and C). Thus, these data indicate that overexpression of Itga3 can dramatically ameliorate ICH-induced NSC pool exhaustion and decreased neurogenesis.

To further examine whether Itga3 overexpression in NSCs could alleviate cognitive impairment post-ICH, we evaluated the cognitive function using water maze and NOR/NOL tests. The results showed that ICH mice with Itga3 overexpression crossed the platform more times, spent less time reaching the platform, stayed in the platform quadrant

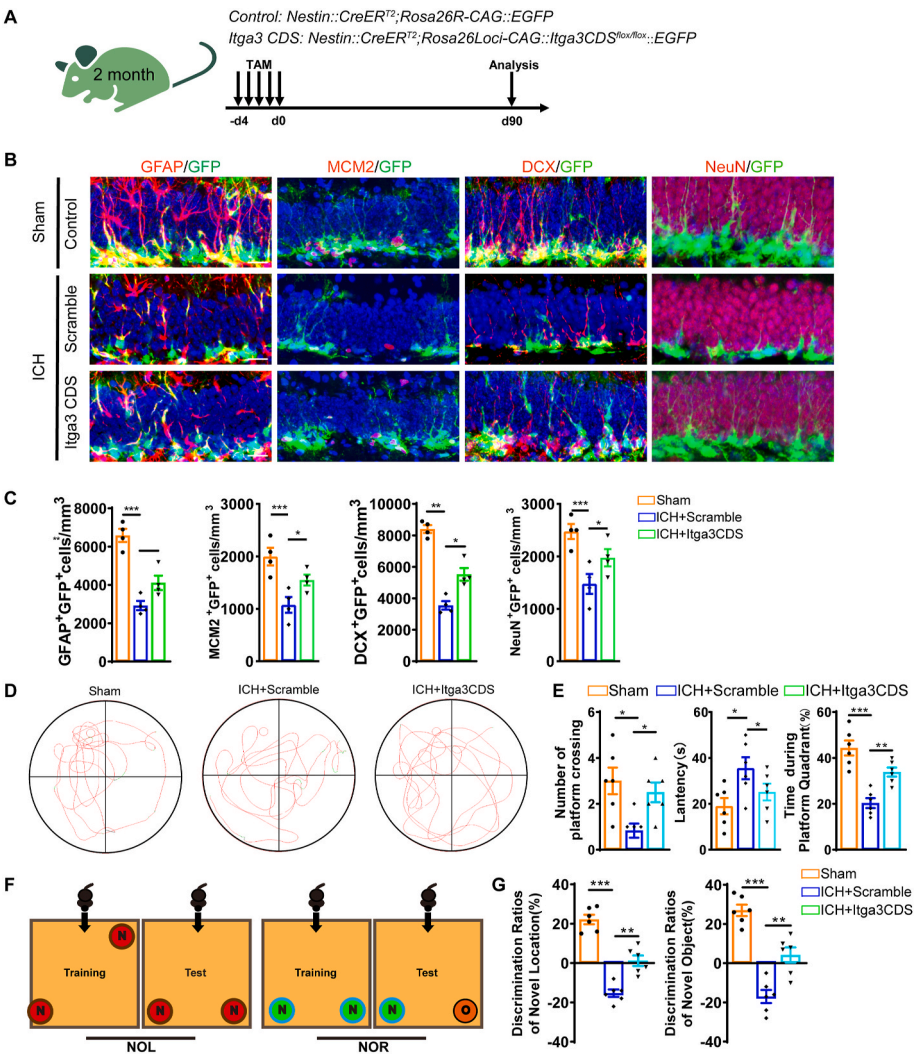

Fig. 7. Conditional overexpression of Itga3 attenuates NSC pool exhaustion and cognitive impairment following ICH (A) Mouse strain and scheme of experimental design. (B) Representative images of brain section stained with GFAP, MCM2, DCX, NeuN and genetically labeled GFP in the DG of Sham, ICH + Scramble and ICH + Itga3CDS group at 90 days after surgical manipulations. Scale bar = 20 μm. (C) The number of rNSCs (GFP^+GFAP^+), proliferating rNSCs (GFP^+MCM2^+), newborn neurons (GFP^+DCX^+) and adult-born neurons (GFP^+NeuN^+) cells at 90 days after ICH, respectively. Conditional overexpression of Itga3 in ICH mice alleviates the decreased neurogenesis induced by ICH. (n = 4 for each group). (D) Representative images of the swimming path of Sham, ICH + Scramble and ICH + Itga3CDS mice during the probe trial test in Morris water maze test at 90 days. Scale bar: 100 μm. (E) Platform-crossing times, escape latency, duration of stay in the platform quadrant of probe trial test from Sham, ICH + Scramble and ICH + Itga3CDS group. (n = 6 for each group). (F) Schematic drawing of novel object location and novel object recognition test. (G) Quantification of the ratio of exploration time on novel objective location and novel objective object in Sham, ICH + Scramble and ICH + Itga3CDS mice. (n = 6 for each group). (C, E, G) *P < 0.05; **P < 0.01; ***P < 0.001 vs corresponding ICH + Scramble. Each experiment was repeated at least 3 times independently.

longer, and spent more time exploring new locations and objects compared to the counterpart ICH group (Fig. 7D–G). Together, the above findings suggest that overexpression of Itga3 could effectively attenuate NSC pool exhaustion and decreased neurogenesis, thereby prevent cognitive impairment following ICH.

4. Discussion

Cognitive impairment after ICH correlates with low quality of life and higher mortality [4–9], while the underlying mechanisms remain largely unclear. Although it is widely accepted that the hippocampus exerts a critical role in cognition [53,54], the involvement of the hippocampus in post-ICH cognitive impairment has yet to be determined. Our study reveals that ICH-induced iron accumulation in the hippocampus elicits the overactivation of NSCs in the early phase, followed by NSC pool depletion and reduced neurogenesis in the chronic phase, which leads to long-term cognitive dysfunction.

Most ICH occurs in the basal ganglion, which is distal to the hippocampus. Iron accumulation in the brain tissue surrounding the hematoma has been observed to be associated with secondary brain injury following ICH [55–57]. However, it remains unclear whether iron deposits in the distal region like hippocampus far from the basal ganglion hematoma. This study encompassed various techniques, including SWI, QSM, and ELISA, to show significant iron accumulation in the hippocampus of patients with ICH, which was also evidenced by the elevated iron level in the CSF of patients.

Previous studies have revealed that iron accumulation is implicated in many brain functions including sensory, motor, and cognitive functions and has been found associated with neurodegenerative diseases and related cognitive decline [58]. However, the mechanisms underlying iron deposit-induced cognitive impairment are not fully understood. Unexpectedly, iron accumulation following ICH influences the activation of NSCs and neurogenesis in the hippocampus. Emerging evidence highlights the significance of adult-born neurons in hippocampal

functions such as learning and memory. The majority of NSCs in the SVZ and DG niches of adult mice are quiescent [12]. Upon activation, these dormant NSCs enter the cell cycle and initiate neurogenesis. Activated adult NSCs play a dual role: self-renewal to maintain their own stem cell pool and the generation of mitotic neural progenitors to expand the precursor population. These progenitors subsequently differentiate into neuroblasts and glial cells, maintaining normal neurogenesis and ensuring homeostasis in the adult brain [11,12].

Previous research conducted by Zhang Bing et al. demonstrated that acute stress exposure in mice led to the rapid depletion of melanocyte stem cells, resulting in premature graying of hair [59]. Similarly, aberrant neurogenesis after epileptic seizures impaires self-renewal ability of hippocampal NSCs, resulting in exhaustion of NSC pool [14,60], indicating abnormal stimulation hampers the reservoir of NSCs. To ensure lifelong neurogenesis and prevent premature exhaustion, NSCs require precise regulation of their quiescence and proliferation processes. Our research findings align with this pattern and suggest that excessive activation of NSCs occurs during the early stages after ICH, followed by depletion of the NSC pool and impaired neurogenesis in the later stages, ultimately leading to cognitive impairment.

Additionally, our data support the idea that the abnormal activation of NSCs following ICH is mainly attributed to iron accumulation in the hippocampus, and the negative effect can be profoundly restored by intervention of DFO and the hypothesis was further validated by the $FeCl_2$ injection to the hippocampus directly. These observations highlight the critical negative role of hippocampal iron accumulation following ICH in maintaining NSC pool and neurogenesis.

ICH can induce iron accumulation, leading to subsequent generation of a significant amount of ROS [61] and the elevated levels of ROS have been implicated in oxidative stress, age-related processes, neurogenesis, and the development of brain dysfunction [62–66]. Targeting ROS has protective effects against a variety of diseases [67–69]. We proposed that iron accumulation after ICH in the hippocampus might induce excessive generation of ROS as well. Our results did show that iron deposition induced ROS accumulation after ICH. This pathological stimulus may trigger the activation of NSCs in the early stages of ICH, ultimately impair neurogenesis.

Integrins are αβ heterodimeric cell surface adhesion receptors that connect the extracellular matrix to the cytoskeleton, and the binding of extracellular matrix ligands to integrins leads to the activation of adhesion-dependent intracellular signaling pathways [70,71], which are mainly correlated with cell proliferation and differentiation. Among them, Integrin α3β1, a key integrin expressed by mammary cells [72,73], plays a significant role in binding primarily to laminins 332 and 511 [74]. Itgb1 was found to be a niche molecule that maintains stem cell homeostasis, and sustains the expansion and self-renewal potential of stem cell pool during regeneration [75], however, the role of Itga3 in the interplay between NSCs and niche microenvironment is still unclear. Our evidence suggests that Itga3 is involved in the regulation of NSC pool and neurogenesis and that the downregulation of Itga3 after ICH might disrupt the integrity of the integrin membrane complex, leading to impaired cell growth and proliferation ability, ultimately contributing to the depletion of the NSC pool. Additionally, from the mechanical point of view, our data reveal that iron-induced excessive ROS accumulation results in sustained chronic oxidative stress, which may contribute to the disrupted composition of the extracellular matrix and downregulation of Itga3 expression. Importantly, downregulation of Itga3 hampers essential cellular processes involved in NSC pool maintenance and neurogenesis. We employed Nestin-CreER^{T2} for lineage tracing and found that conditional overexpression of Itga3 in ICH mice obviously restored neurogenesis in the hippocampus, preserved the balance and stability of the NSC pool, leading to better performance in behavioral tests.

Besides, our findings highlight the effectiveness of the iron-chelating agent DFO in mitigating the exhaustion of hippocampal NSC pool. Although i-DEF trial fail to improve the chance of good clinical outcome (mRS score of 0–2) at day 90 [76], our data suggest that DFO may be a promising drug for maintaining the NSC pool, enhancing normal neurogenesis and preventing post-ICH cognitive impairments.

In summary, our study for the first time provides insights into the impact of hippocampal iron accumulation on the cognition following ICH. Mechanistically, iron accumulation leads to elevated ROS level, downregulated Itga3, depletion of the NSC pool, and subsequent impairments of neurogenesis, ultimately resulting in cognitive dysfunction. These findings extend our understanding how ICH-induced iron accumulation links with NSC pool and identify potential targets for the prevention of post-ICH cognitive impairment.

Authors' contributions

Xuyang Zhang and Huanhuan Li performed most of the experiments with assistance from Chao Guo, Qian Zhang, Hui Feng, Fengchun Zhao, Jun Zhong and Hua Feng. Xueyun Deng and Wei Chen performed SWI and QSM analysis. Xuyang Zhang, Haomiao Wang and Jun Zhang conducted the statistical analysis and prepared the figures. Haomiao Wang, Yi Yin, Jun Zhang and Xuyang Zhang conducted bioinformatics analysis and literature review. Tengyuan Zhou, Hua Feng and Yi Yin performed the immunoblotting and immunostaining. Xuyang Zhang and Haomiao Wang wrote the preliminary draft of the manuscript. Rong Hu conceived this project, designed all the experiments and revised the manuscript. All authors approved the final version of the manuscript.

CRediT authorship contribution statement

Xuyang Zhang: Writing – original draft, Visualization, Validation, Software, Resources, Methodology, Investigation, Formal analysis, Data curation. **Huanhuan Li:** Validation, Resources, Methodology, Investigation, Data curation. **Haomiao Wang:** Writing – original draft, Visualization, Software, Investigation, Funding acquisition, Formal analysis. **Qian Zhang:** Resources, Project administration, Methodology, Data curation. **Xueyun Deng:** Resources, Methodology, Investigation, Data curation. **Shuixian Zhang:** Resources, Project administration, Methodology, Data curation. **Long Wang:** Resources, Methodology, Data curation. **Chao Guo:** Validation, Resources, Methodology, Investigation, Data curation. **Fengchun Zhao:** Validation, Methodology, Investigation, Data curation. **Yi Yin:** Resources, Methodology, Investigation, Data curation. **Tengyuan Zhou:** Validation, Methodology, Investigation, Data curation. **Jun Zhong:** Resources, Methodology, Investigation, Data curation. **Hui Feng:** Validation, Resources, Methodology, Investigation, Data curation. **Wei Chen:** Validation, Supervision, Resources, Formal analysis, Data curation. **Jun Zhang:** Validation, Supervision, Software, Resources, Methodology, Investigation, Formal analysis, Data curation. **Hua Feng:** Writing – review & editing, Supervision, Conceptualization. **Rong Hu:** Writing – review & editing, Supervision, Project administration, Funding acquisition, Conceptualization.

Declaration of competing interest

The authors declare that there are no conflicts of interest.

Data availability

Data will be made available on request.

Acknowledgments

This work was supported by grants from the National Natural Science Foundation of China (81671228 to R.H.), Chongqing Municipal Science Fund for Distinguished Young Scholars (cstc2019jcyjjqX0030 to R.H.) and National College Students' innovation and entrepreneurship training program (202290031034 to HM.W.).

Appendix A. Supplementary data

Supplementary data to this article can be found online at https://doi.org/10.1016/j.redox.2024.103086.

References

[1] M. D, B. EJ, G. AS, A. DK, B. MJ, C. M, D. SR, d.F. S, D. JP, F. HJ, et al., Heart disease and stroke statistics-2016 update: a report from the American heart association, Circulation 133 (2016), https://doi.org/10.1161/cir.0000000000000350 e38-360.

[2] H. Jc, G. SM, A. CS, B. K, B. BR, C. M, F. GL, G. JN, M. RL, M. PH, et al., Guidelines for the management of spontaneous intracerebral hemorrhage: a guideline for healthcare professionals from the American heart association/American stroke association, Stroke 46 (2015) 2032–2060, https://doi.org/10.1161/str.0000000000000069.

[3] L. Puy, A. Parry-Jones, E. Sandset, D. Dowlatshahi, W. Ziai, C. Cordonnier, Intracerebral haemorrhage, Nat. Rev. Dis. Prim. 9 (2023) 14, https://doi.org/10.1038/s41572-023-00424-7.

[4] S. Kazim, J. Ogulnick, M. Robinson, J. Eliyas, B. Spangler, T. Hough, E. Martinez, Z. Karimov, D. Vidrine, M. Schmidt, C. Bowers, Cognitive impairment after intracerebral hemorrhage: a systematic review and meta-analysis, World neurosurgery 148 (2021) 141–162, https://doi.org/10.1016/j.wneu.2021.01.026.

[5] K. Murao, C. Rossi, C. Cordonnier, Intracerebral haemorrhage and cognitive decline, Rev. Neurol. 169 (2013) 772–778, https://doi.org/10.1016/j.neurol.2013.07.021.

[6] M. Pasi, L. Sugita, L. Xiong, A. Charidimou, G. Boulouis, T. Pongpitakmetha, S. Singh, C. Kourkoulis, K. Schwab, S. Greenberg, et al., Association of cerebral small vessel disease and cognitive decline after intracerebral hemorrhage, Neurology 96 (2021) e182–e192, https://doi.org/10.1212/wnl.0000000000011050.

[7] E. Smith, M. Gurol, J. Eng, C. Engel, T. Nguyen, J. Rosand, S. Greenberg, White matter lesions, cognition, and recurrent hemorrhage in lobar intracerebral hemorrhage, Neurology 63 (2004) 1606–1612, https://doi.org/10.1212/01.wnl.0000142966.22886.20.

[8] A. Viswanathan, P. Patel, R. Rahman, R. Nandigam, C. Kinnecom, L. Bracoud, J. Rosand, H. Chabriat, S. Greenberg, E. Smith, Tissue microstructural changes are independently associated with cognitive impairment in cerebral amyloid angiopathy, Stroke 39 (2008) 1988–1992, https://doi.org/10.1161/strokeaha.107.509091.

[9] J. Attems, F. Lauda, K. Jellinger, Unexpectedly low prevalence of intracerebral hemorrhages in sporadic cerebral amyloid angiopathy: an autopsy study, J. Neurol. 255 (2008) 70–76, https://doi.org/10.1007/s00415-008-0674-4.

[10] T. Potter, V. Lioutas, M. Tano, A. Pan, J. Meeks, D. Woo, S. Seshadri, M. Selim, F. Vahidy, Cognitive impairment after intracerebral hemorrhage: a systematic review of current evidence and knowledge gaps, Front. Neurol. 12 (2021) 716632, https://doi.org/10.3389/fneur.2021.716632.

[11] M. Bonaguidi, M. Wheeler, J. Shapiro, R. Stadel, G. Sun, G. Ming, H. Song, In vivo clonal analysis reveals self-renewing and multipotent adult neural stem cell characteristics, Cell 145 (2011) 1142–1155, https://doi.org/10.1016/j.cell.2011.05.024.

[12] A. Bond, G. Ming, H. Song, Adult mammalian neural stem cells and neurogenesis: five decades later, Cell Stem Cell 17 (2015) 385–395, https://doi.org/10.1016/j.stem.2015.09.003.

[13] J. Wang, Y. Cui, Z. Yu, W. Wang, X. Cheng, W. Ji, S. Guo, Q. Zhou, N. Wu, Y. Chen, et al., Brain endothelial cells maintain lactate homeostasis and control adult hippocampal neurogenesis, Cell Stem Cell 25 (2019) 754–767, https://doi.org/10.1016/j.stem.2019.09.009, e759.

[14] C.H. Fu, D.M. Iascone, I. Petrof, A. Hazra, J. Chin, Early seizure activity accelerates depletion of hippocampal neural stem cells and impairs spatial discrimination in an alzheimer's disease model, Cell Rep. 27 (2019) 3741–3751, e3744.

[15] D. Ma, M. Bonaguidi, G. Ming, H. Song, Adult neural stem cells in the mammalian central nervous system, Cell Res. 19 (2009) 672–682, https://doi.org/10.1038/cr.2009.56.

[16] J. Gonçalves, S. Schafer, F. Gage, Adult neurogenesis in the Hippocampus: from stem cells to behavior, Cell 167 (2016) 897–914, https://doi.org/10.1016/j.cell.2016.10.021.

[17] J. Chen, X.Y. Yuan, X. Zhang, Intracerebral Hemorrhage Influences Hippocampal Neurogenesis and Neurological Function Recovery via Notch 1 Signaling, 2021. NeuroReport *publish ahead of print*.

[18] T. Masuda, Y. Isobe, N. Aihara, F. Furuyama, H. Hida, Increase in neurogenesis and neuroblast migration after a small intracerebral hemorrhage in rats, Neurosci. Lett. 425 (2007) 114–119.

[19] L. Otero, M. Zurita, C. Bonilla, M. Rico, C. Aguayo, A. Rodriguez, J. Vaquero, Endogenous neurogenesis after intracerebral hemorrhage, Histol. Histopathol. 27 (2012) 303–315, https://doi.org/10.14670/hh-27.303.

[20] A. Topiwala, C. Wang, K. Ebmeier, S. Burgess, S. Bell, D. Levey, H. Zhou, C. McCracken, A. Roca-Fernández, S. Petersen, et al., Associations between moderate alcohol consumption, brain iron, and cognition in UK Biobank participants: observational and mendelian randomization analyses, PLoS Med. 19 (2022) e1004039, https://doi.org/10.1371/journal.pmed.1004039.

[21] L. Zecca, M. Youdim, P. Riederer, J. Connor, R. Crichton, Iron, brain ageing and neurodegenerative disorders, Nat. Rev. Neurosci. 5 (2004) 863–873, https://doi.org/10.1038/nrn1537.

[22] M. Hentze, M. Muckenthaler, B. Galy, C. Camaschella, Two to tango: regulation of Mammalian iron metabolism, Cell 142 (2010) 24–38, https://doi.org/10.1016/j.cell.2010.06.028.

[23] T. Moos, E. Morgan, The metabolism of neuronal iron and its pathogenic role in neurological disease: review, Ann. N. Y. Acad. Sci. 1012 (2004) 14–26, https://doi.org/10.1196/annals.1306.002.

[24] G. Yang, C. Qian, C. Zhang, Y. Bao, M. Liu, F. Jiang, W. Li, Y. Liu, Y. Ke, Z. Qian, Hepcidin attenuates the iron-mediated secondary neuronal injury after intracerebral hemorrhage in rats, Transl. Res. : J. Lab. Clin. Med. 229 (2021) 53–68, https://doi.org/10.1016/j.trsl.2020.09.002.

[25] J. Tang, Q. Chen, J. Guo, L. Yang, Y. Tao, L. Li, H. Miao, H. Feng, Z. Chen, G. Zhu, Minocycline attenuates neonatal germinal-matrix-hemorrhage-induced neuroinflammation and brain edema by activating cannabinoid receptor 2, Mol. Neurobiol. 53 (2016) 1935–1948, https://doi.org/10.1007/s12035-015-9154-x.

[26] X. Zhang, Z. Liu, W. Yang, F. Zhao, C. Zhang, H. Feng, T. Zhou, J. Zhong, Y. Zou, H. Feng, et al., Tetrahydrofolate alleviates the inhibitory effect of oxidative stress on neural stem cell proliferation through PTEN/Akt/mTOR pathway, Oxid. Med. Cell. Longev. 2022 (2022) 9021474, https://doi.org/10.1155/2022/9021474.

[27] W. Yang, N. Ding, R. Luo, Q. Zhang, Z. Li, F. Zhao, S. Zhang, X. Zhang, T. Zhou, H. Wang, et al., Exosomes from young healthy human plasma promote functional recovery from intracerebral hemorrhage via counteracting ferroptotic injury, Bioact. Mater. 27 (2023) 1–14, https://doi.org/10.1016/j.bioactmat.2023.03.007.

[28] Z. Zhang, P. Guo, L. Liang, S. Jila, X. Ru, Q. Zhang, J. Chen, Z. Chen, H. Feng, Y. Chen, NLRP3-dependent lipid droplet formation contributes to posthemorrhagic hydrocephalus by increasing the permeability of the blood-cerebrospinal fluid barrier in the choroid plexus, Exp. Mol. Med. 55 (2023) 574–586, https://doi.org/10.1038/s12276-023-00955-9.

[29] Y. Yang, K. Zhang, X. Chen, C. Yang, J. Wang, X. Lei, Y. Quan, W. Chen, H. Zhao, L. Yang, et al., Cyclophilin D-induced mitochondrial impairment confers axonal injury after intracerebral hemorrhage in mice, Neural regeneration research 18 (2023) 849–855, https://doi.org/10.4103/1673-5374.353495.

[30] J. Lin, Y. Xu, P. Guo, Y. Chen, J. Zhou, M. Xia, B. Tan, X. Liu, H. Feng, Y. Chen, CCL5/CCR5-mediated peripheral inflammation exacerbates blood–brain barrier disruption after intracerebral hemorrhage in mice, J. Transl. Med. 21 (2023) 196, https://doi.org/10.1186/s12967-023-04044-3.

[31] J. Wang, X. Tang, M. Xia, C. Li, C. Guo, H. Ge, Y. Yin, B. Wang, W. Chen, H. Feng, Iron chelation suppresses secondary bleeding after intracerebral hemorrhage in angiotensin II-infused mice, CNS Neurosci. Ther. 27 (2021) 1327–1338, https://doi.org/10.1111/cns.13706.

[32] W. Chen, C. Guo, H. Feng, Y. Chen, Mitochondria: novel mechanisms and therapeutic targets for secondary brain injury after intracerebral hemorrhage, Front. Aging Neurosci. 12 (2020) 615451, https://doi.org/10.3389/fnagi.2020.615451.

[33] W. Chen, C. Guo, S. Huang, Z. Jia, J. Wang, J. Zhong, H. Ge, J. Yuan, T. Chen, X. Liu, et al., MitoQ attenuates brain damage by polarizing microglia towards the M2 phenotype through inhibition of the NLRP3 inflammasome after ICH, Pharmacol. Res. 161 (2020) 105122, https://doi.org/10.1016/j.phrs.2020.105122.

[34] S. You, X. Wang, R. Lindley, T. Robinson, C. Anderson, Y. Cao, J. Chalmers, Early cognitive impairment after intracerebral hemorrhage in the INTERACT1 study, Cerebrovasc. Dis. (2017) 320–324.

[35] A. Douiri, A.G. Rudd, C.D.A. Wolfe, Prevalence of poststroke cognitive impairment: south London stroke register 1995-2010, Stroke 44 (2012) 138–145.

[36] M.R. Benedictus, H. Anais, Costanza Rossi, Gregoire Boulouis, Hildevan Henon, Wiesje M. der Flier, Charlotte Cordonnier, Prognostic factors for cognitive decline after intracerebral hemorrhage, Stroke: A Journal of Cerebral Circulation 46 (2015).

[37] C. Liu, C. Li, J. Yang, L. Gui, L. Zhao, A. Evans, X. Yin, J. Wang, Characterizing brain iron deposition in subcortical ischemic vascular dementia using susceptibility-weighted imaging: an in vivo MR study, Behav. Brain Res. 288 (2015) 33–38, https://doi.org/10.1016/j.bbr.2015.04.003.

[38] S. Yao, Y. Zhong, Y. Xu, J. Qin, N. Zhang, X. Zhu, Y. Li, Quantitative susceptibility mapping reveals an association between brain iron load and depression severity, Front. Hum. Neurosci. 11 (2017) 442, https://doi.org/10.3389/fnhum.2017.00442.

[39] H. Ge, T. Zhou, C. Zhang, Y. Cun, W. Chen, Y. Yang, Q. Zhang, H. Li, J. Zhong, X. Zhang, et al., Targeting ASIC1a promotes neural progenitor cell migration and neurogenesis in ischemic stroke, Research 6 (2023) 0105, https://doi.org/10.34133/research.0105.

[40] G. Yang, R. Hu, C. Zhang, C. Qian, Q. Luo, W. Yung, Y. Ke, H. Feng, Z. Qian, A combination of serum iron, ferritin and transferrin predicts outcome in patients with intracerebral hemorrhage, Sci. Rep. 6 (2016) 21970, https://doi.org/10.1038/srep21970.

[41] ST Pendlebury, J Mariz, L Bull, Z Mehta, PM Rothwell, MoCA, ACE-R, and MMSE versus the National Institute of Neurological Disorders and Stroke-Canadian stroke network vascular cognitive impairment harmonization standards neuropsychological battery after TIA and stroke, Stroke 43 (2) (2012) 464, 9.

[42] P.M. Rothwell, S.T. Pendlebury, Z. Mehta, L. Bull, J. Mariz, MoCA, ACE-R, and MMSE versus the national institute of neurological disorders and stroke-Canadian stroke network vascular cognitive impairment harmonization standards neuropsychological battery after TIA and stroke, Stroke 43 (2) (2018) 464–469, 2012.

[43] Y. Dong, V.K. Sharma, B.P.-L. Chan, N. Venketasubramanian, H.L. Teoh, R.C. S. Seet, S. Tanicala, Y.H. Chan, C. Chen, The Montreal Cognitive Assessment (MoCA) is superior to the Mini-Mental State Examination (MMSE) for the detection

of vascular cognitive impairment after acute stroke, J. Neurol. Sci. 299 (1-2) (2010) 15–18, 12; 15.
[44] A. Aggarwal, E. Kean, Comparison of the folstein mini mental state examination (MMSE) to the Montreal cognitive assessment (MoCA) as a cognitive screening tool in an inpatient rehabilitation setting, Neurosci. Med. 1 (2010) 39–42.
[45] K. Jellinger, Pathology of intracerebral hemorrhage, Zentralbl. Neurochir. 38 (1977) 29–42.
[46] B. JP, B. T, T. T, M. R, H. G, Intracerebral hemorrhage more than twice as common as subarachnoid hemorrhage, J. Neurosurg. 78 (1993) 188–191, https://doi.org/10.3171/jns.1993.78.2.0188.
[47] Q. Chen, J. Tang, L. Tan, J. Guo, Y. Tao, L. Li, Y. Chen, X. Liu, J. Zhang, Z. Chen, H. Feng, Intracerebral hematoma contributes to hydrocephalus after intraventricular hemorrhage via aggravating iron accumulation, Stroke 46 (2015) 2902–2908, https://doi.org/10.1161/strokeaha.115.009713.
[48] H. Song, C.F. Stevens, F.H. Gage, Astroglia induce neurogenesis from adult neural stem cells, Nature 417 (2002) 39–44.
[49] D.K. Ma, M.H. Jang, J.U. Guo, Y. Kitabatake, M.L. Chang, N. Pow-Anpongkul, R. A. Flavell, B. Lu, G.L. Ming, H. Song, Neuronal activity–induced Gadd45b promotes epigenetic DNA demethylation and adult neurogenesis, Science 323 (2009) 1074–1077.
[50] C. Xu, Y. Pan, H. Zhang, Y. Sun, Y. Cao, P. Qi, M. Li, O. Akakuru, L. He, C. Xiao, et al., Platelet-membrane-coated polydopamine nanoparticles for neuroprotection by reducing oxidative stress and repairing damaged vessels in intracerebral hemorrhage, Adv. Healthcare Mater. 12 (2023) e2300797, https://doi.org/10.1002/adhm.202300797.
[51] M. Wang, C. Zhou, L. Yu, D. Kong, W. Ma, B. Lv, Y. Wang, W. Wu, M. Zhou, G. Cui, Upregulation of MDH1 acetylation by HDAC6 inhibition protects against oxidative stress-derived neuronal apoptosis following intracerebral hemorrhage, Cell. Mol. Life Sci. : CM 79 (2022) 356, https://doi.org/10.1007/s00018-022-04341-y.
[52] E. Tomellini, I. Fares, B. Lehnertz, J. Chagraoui, N. Mayotte, T. MacRae, M. Bordeleau, S. Corneau, R. Bisaillon, G. Sauvageau, Integrin-α3 is a functional marker of ex vivo expanded human long-term hematopoietic stem cells, Cell Rep. 28 (2019) 1063–1073, https://doi.org/10.1016/j.celrep.2019.06.084, e1065.
[53] J. Lisman, G.r. Buzsáki, H. Eichenbaum, L. Nadel, C. Rangananth, A.D. Redish, Viewpoints: how the hippocampus contributes to memory, navigation and cognition, Nat. Neurosci. 20 (2017) 1434.
[54] X. Han, S. Huang, Z. Zhuang, X. Zhang, M. Xie, N. Lou, M. Hua, X. Zhuang, S. Yu, S. Chen, Phosphatidate phosphatase Lipin 1 involves in diabetic encephalopathy pathogenesis via regulating synaptic mitochondrial dynamics, Redox Biol. 69 (2024) 102996, https://doi.org/10.1016/j.redox.2023.102996.
[55] X. Xiong, L. Liu, F. Wang, Y. Yang, J. Hao, P. Wang, Q. Zhong, K. Zhou, A. Xiong, W. Zhu, et al., Toll-like receptor 4/MyD88-mediated signaling of hepcidin expression causing brain iron accumulation, oxidative injury, and cognitive impairment after intracerebral hemorrhage, Circulation 134 (2016) 1025–1038, https://doi.org/10.1161/circulationaha.116.021881.
[56] X. Xiong, J. Wang, Z. Qian, Q. Yang, Iron and intracerebral hemorrhage: from mechanism to translation, Translational stroke research 5 (2014) 429–441, https://doi.org/10.1007/s12975-013-0317-7.
[57] Y. Gong, J. Deng, Y. Wu, X. Xu, Z. Hou, S. Hao, B. Wang, Role of mass effect on neuronal iron deposition after intracerebral hemorrhage, Exp. Neurol. 368 (2023) 114475, https://doi.org/10.1016/j.expneurol.2023.114475.
[58] H. Tang, A. Manaenko, Y. He, S. Tang, Y. Ou, The role of iron, its metabolism and ferroptosis in traumatic brain injury, Front. Cell. Neurosci. 14 (2020).
[59] B. Zhang, S. Ma, I. Rachmin, M. He, P. Baral, S. Choi, W.A. Gonalves, Y. Shwartz, E. M. Fast, Y. Su, Hyperactivation of sympathetic nerves drives depletion of melanocyte stem cells, Nature 577 (1) (2020) 676–681 (7792).
[60] H. Noguchi, J. Arela, T. Ngo, L. Cocas, S. Pleasure, Shh from mossy cells contributes to preventing NSC pool depletion after seizure-induced neurogenesis and in aging, bioRxiv : the preprint server for biology (2023), https://doi.org/10.1101/2023.08.21.554173.
[61] J. Wan, H. Ren, J. Wang, Iron toxicity, lipid peroxidation and ferroptosis after intracerebral haemorrhage, Stroke and vascular neurology 4 (2019) 93–95, https://doi.org/10.1136/svn-2018-000205.
[62] C. Massaad, E. Klann, Reactive oxygen species in the regulation of synaptic plasticity and memory, Antioxidants Redox Signal. 14 (2011) 2013–2054, https://doi.org/10.1089/ars.2010.3208.
[63] L. Lavie, Oxidative stress in obstructive sleep apnea and intermittent hypoxia-revisited-the bad ugly and good: implications to the heart and brain, Sleep Med. Rev. 20 (2015) 27–45, https://doi.org/10.1016/j.smrv.2014.07.003.
[64] J. Chang, B. Guo, Y. Gao, W. Li, X. Tong, Y. Feng, N. Abumaria, Characteristic features of deep brain lymphatic vessels and their regulation by chronic stress, Research 6 (2023) 0120, https://doi.org/10.34133/research.0120.
[65] B. Zhang, L. Wang, A. Zhan, M. Wang, L. Tian, W. Guo, Y. Pan, Long-term exposure to a hypomagnetic field attenuates adult hippocampal neurogenesis and cognition, Nat. Commun. 12 (2021) 1174, https://doi.org/10.1038/s41467-021-21468-x.
[66] Z. He, X. Li, Z. Wang, Y. Cao, S. Han, N. Li, J. Cai, S. Cheng, Q. Liu, Protective effects of luteolin against amyloid beta-induced oxidative stress and mitochondrial impairments through peroxisome proliferator-activated receptor γ-dependent mechanism in Alzheimer's disease, Redox Biol. 66 (2023) 102848, https://doi.org/10.1016/j.redox.2023.102848.
[67] G. Cheng, X. Liu, Y. Liu, Y. Liu, R. Ma, J. Luo, X. Zhou, Z. Wu, Z. Liu, T. Chen, Y. Yang, Ultrasmall Coordination Polymers for Alleviating ROS-Mediated Inflammatory and Realizing Neuroprotection against Parkinson's Disease, 2022 9781323, https://doi.org/10.34133/2022/9781323. Research (Washington, D.C.) 2022.
[68] W. Yang, H. Yue, G. Lu, W. Wang, Y. Deng, G. Ma, W. Wei, Advances in delivering oxidative modulators for disease therapy, Research (2022), https://doi.org/10.34133/2022/9897464, 2022.
[69] J. Tang, L. Huang, J. Deng, Y. Wang, C. Guo, X. Peng, Z. Liu, J. Gao, Cognitive enhancement and neuroprotective effects of OABL, a sesquiterpene lactone in 5xFAD Alzheimer's disease mice model, Redox Biol. 50 (2022) 102229, https://doi.org/10.1016/j.redox.2022.102229.
[70] R. Hynes, Integrins: bidirectional, allosteric signaling machines, Cell 110 (2002) 673–687, https://doi.org/10.1016/s0092-8674(02)00971-6.
[71] S. Huveneers, E. Danen, Adhesion signaling - crosstalk between integrins, Src and Rho, J. Cell Sci. 122 (2009) 1059–1069, https://doi.org/10.1242/jcs.039446.
[72] O. Paavolainen, E. Peuhu, Integrin-mediated adhesion and mechanosensing in the mammary gland, Semin. Cell Dev. Biol. 114 (2021) 113–125, https://doi.org/10.1016/j.semcdb.2020.10.010.
[73] C. Förster, S. Mäkela, A. Wärri, S. Kietz, D. Becker, K. Hultenby, M. Warner, J. Gustafsson, Involvement of estrogen receptor beta in terminal differentiation of mammary gland epithelium, Proc. Natl. Acad. Sci. U.S.A. 99 (2002) 15578–15583, https://doi.org/10.1073/pnas.192561299.
[74] E. Bae, P. Huang, G. Müller-Greven, D. Hambardzumyan, A. Sloan, A. Nowacki, N. Marko, C. Carlin, C. Gladson, Integrin α3β1 promotes vessel formation of glioblastoma-associated endothelial cells through calcium-mediated macropinocytosis and lysosomal exocytosis, Nat. Commun. 13 (2022) 4268, https://doi.org/10.1038/s41467-022-31981-2.
[75] M. Rozo, L. Li, C. Fan, Targeting β1-integrin signaling enhances regeneration in aged and dystrophic muscle in mice, Nat. Med. 22 (2016) 889–896, https://doi.org/10.1038/nm.4116.
[76] M. Selim, L. Foster, C. Moy, G. Xi, M. Hill, L. Morgenstern, S. Greenberg, M. James, V. Singh, W. Clark, et al., Deferoxamine mesylate in patients with intracerebral haemorrhage (i-DEF): a multicentre, randomised, placebo-controlled, double-blind phase 2 trial, Lancet Neurol. 18 (2019) 428–438, https://doi.org/10.1016/s1474-4422(19)30069-9.